

1 **Rescue of Conformational Dynamics in Enzyme Catalysis by Directed Evolution**

2

3 Renee Otten^{1,#}, Lin Liu^{2,#}, Lillian R. Kenner², Michael W. Clarkson^{1,†}, David Mavor², Dan S.

4 Tawfik³, Dorothee Kern^{1,*}, James S. Fraser^{2,*}

5

6 ¹Howard Hughes Medical Institute and Department of Biochemistry, Brandeis University, 415 South Street,

7 Waltham, MA 02454, USA

8 ²Department of Bioengineering and Therapeutic Sciences, University of California San Francisco, San Francisco,

9 CA 94158, USA

10 ³Department of Biomolecular Sciences, Weizmann Institute of Science, Rehovot, Israel

11 [†]Present address: Biological Sciences West, The University of Arizona, 1041 E Lowell Street, Tucson, AZ 85721,

12 USA

13 [#]these authors contributed equally to this work

14

15

16 **Abstract**

17 Rational design and directed evolution have proved to be successful approaches to increase
18 catalytic efficiencies of both natural and artificial enzymes¹⁻³. However, a comprehensive
19 understanding of how evolution shapes the energy landscape of catalysis remains a fundamental
20 challenge. Protein dynamics is widely recognized as important, but due to the inherent flexibility
21 of biological macromolecules it is often difficult to distinguish which conformational changes are
22 directly related to function. Here, we used directed evolution on an impaired mutant of the human
23 proline isomerase cyclophilin A (CypA) and identify two second-shell mutations that partially
24 restore its catalytic activity. We show both kinetically, using NMR spectroscopy, and structurally,
25 by room-temperature X-ray crystallography, how local perturbations propagate through a large
26 allosteric network to facilitate conformational dynamics. The increased catalysis selected for in
27 the evolutionary screen could be rationalized entirely by accelerated interconversion between the
28 two catalytically essential conformational sub-states, which are both captured in the high-
29 resolution X-ray ensembles at room temperature. Our data provide a glimpse of the evolutionary
30 trajectory of an enzyme's energy landscape and shows how subtle changes can fine-tune its
31 function.

32

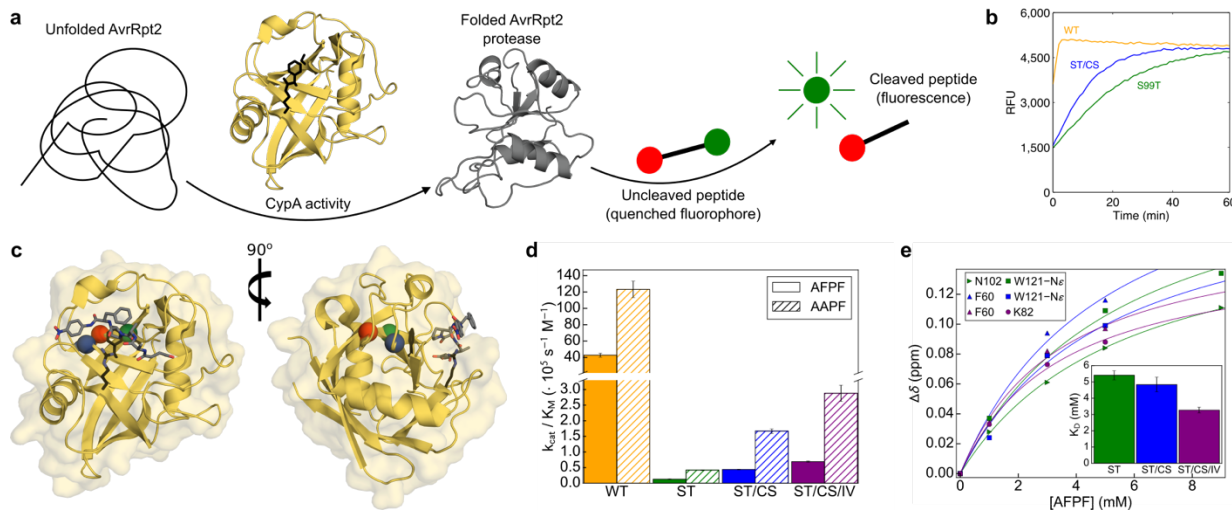
33 The importance of protein dynamics in enzyme function has been under extensive investigation
34 by experimental and computational methods and has become more widely accepted⁴⁻⁸. However,
35 because proteins are inherently flexible, assigning a direct functional role to specific
36 conformational changes has proved challenging. For human peptidyl-prolyl cis/trans isomerase
37 CypA, a combination of biophysical experimental techniques has elucidated general principles of
38 the energy landscape during catalysis⁹⁻¹¹. Since evolutionary selection acts on function, a new
39 challenge is to understand how evolution shapes these energy landscapes¹². This challenge is best

40 exemplified by the common implication of protein dynamics as speculative explanation for the
41 impressive functional improvements achieved via directed evolution where often only minimal
42 structural changes are observed^{1,13}. Here, we experimentally characterize changes in the energy
43 landscape that emerge from directed evolution of CypA for enhanced catalytic activity. We find a
44 direct correspondence of increased protein dynamics and faster catalysis along an evolutionary
45 trajectory.

46

47 To directly observe the changes in an enzyme's energy landscape upon directed evolution, we
48 turned to a previously designed second-shell mutation, S99T, in CypA that had three effects:
49 inverting the equilibrium between two states that are essential for catalysis, decreasing their
50 interconversion rate, and causing a parallel reduction in catalysis¹¹. Can we restore the catalytic
51 function via directed evolution and discern how the acquired mutations compensate for the
52 impaired conformational dynamics of the S99T mutant at the molecular level? To enable directed
53 evolution on S99T CypA, first a 96-well plate screen was developed that reports on the enzymatic
54 activity of CypA. Proline isomerase activity is difficult to screen because of its high thermal
55 background rate ($2\text{--}9 \times 10^{-3} \text{ s}^{-1}$)^{14,15}. Additionally, there are several proline isomerases in
56 *Escherichia coli*, which complicates screening in cell lysate. To overcome these limitations, we
57 took advantage of the *Pseudomonas syringae* phytopathogenic protease AvrRpt2, which is
58 activated by eukaryotic, but not prokaryotic, cyclophilin homologs¹⁶. We expressed a library of
59 CypA S99T variants created by random mutagenesis, added inactive AvrRpt2 to cell lysate and
60 monitored the cleavage of an AvrRpt2 substrate¹⁷ (Fig. 1a). Besides revertants to wild-type CypA
61 (Ser99), we identified a variant (S99T/C115S) with increased activity (Fig. 1b). A second round
62 of screening of S99T/C115S CypA identified an additional mutation (I97V) with a further increase

63 in activity. Extensive efforts to further improve enzymatic activity by many more rounds of
 64 evolution were unsuccessful. Both gain-of-function mutations are in proximity of Thr99, but not
 65 in direct contact with the peptide substrate (Fig. 1c). Each mutation contributes additively to the
 66 increase in activity, measured as k_{cat}/K_M^{18} , and is consistent across two substrate peptides (Fig.
 67 1d). Substrate binding affinities are only slightly changed relative to the S99T mutant (Fig. 1e and
 68 Extended Data Fig. 2) suggesting that the two mutations function by modulating the turnover rate
 69 rather than substrate binding.



70
 71
 72 **Figure 1 | Directed Evolution selects rescue mutations for catalysis.**
 73 (a) Scheme of the assay used in directed evolution to identify CypA mutations with increased
 74 catalytic activity: CypA activity for folding of AvrRpt2 protease measured by AvrRpt2-mediated
 75 cleavage of the peptide Abz-IEAPAFGGWy-NH₂ ($\gamma = 3$ -nitro-Tyrosine). (b) Assay of directed
 76 evolution performed on cell lysate in 96-well plates to identify rescue mutations for S99T with
 77 increased CypA activity. Kinetics of peptide cleavage is shown for wild-type (yellow), S99T
 78 (green) and S99T/C115S (blue) CypA. (c) Sites of mutations are plotted onto the crystal structure (1RMH²⁹) of CypA bound to Suc-AAPF-pNA (grey sticks)
 79 and the active-site residues R55 and F113 are shown in black stick representation. The overlay of
 80 NMR spectra shows that the overall structure of all CypA forms is very similar, with perturbations
 81 observed for residues close to the mutation site or in the dynamic network (Extended Data Fig. 1).
 82 (d) k_{cat}/K_M values for wild-type, S99T, S99T/C115S and S99T/C115S/I97V CypA measured by
 83 protease coupled hydrolysis¹⁸ of Suc-AFPF-pNA and Suc-AAPF-pNA peptides. Error bars
 84 indicate the standard deviation obtained from triplicate measurements on at least three different
 85 enzyme concentrations. (e) K_D values for the three mutant forms of CypA for Suc-AFPF-pNA
 86 measured by NMR chemical shift analysis from peptide titrations (see also Extended Data Fig. 2).
 87 Error bars denote the standard errors in the fitted parameters obtained from the global fit.
 88

90 To determine whether the rescue in catalysis is due to faster protein motion, we performed NMR
91 dynamics experiments on the S99T, S99T/C115S and S99T/C115S/I97V mutants (Fig. 2 and
92 Supplementary Data 1-6). Previous NMR CPMG dispersion experiments suggested a direct link
93 between the speed of a conformational change in a dynamic network, labeled group-I, for both
94 wild-type (WT) and S99T CypA (Fig. 2a, red)^{10,11}. In contrast, a second dynamic process, group-
95 II, comprised of loops adjacent to the active site (Fig. 2a, blue), is insensitive to mutation and
96 displayed faster dynamics. Despite the lack of correlation between the dynamics and catalysis in
97 the group-II residues in S99T, these residues have recently been proposed to be directly linked to
98 catalysis in CypA¹⁹. To understand the changes in the energy landscape during the directed
99 evolution that led to faster enzymes, we first turned to well-established ¹⁵N-CMPG experiments.
100 Interestingly, the exchange contribution, R_{ex} , for group-I residues gets bigger with consecutive
101 rescue mutations (Fig. 2b), indicating that these mutations increase the slow interconversion rate
102 from the major to minor state (i.e., $R_{ex} = k_{maj \rightarrow min}$). We note that the fast loop motion of group-II
103 (residues 65-80) is observed in all enzyme forms and remains essentially unaltered (Fig. 2a-c,e,g
104 and Supplementary Data 1-3).

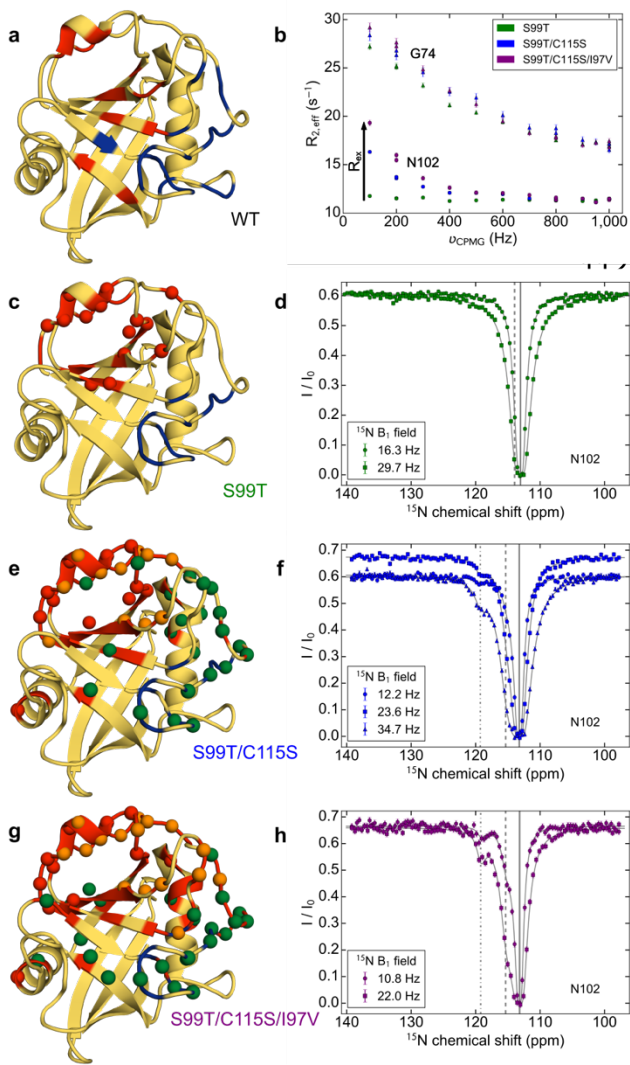


Figure 2 | Rescue mutants alter the conformational dynamics of CypA as measured by NMR.

(a) Dynamics on WT CypA (shown here)¹⁰ and S99T¹¹ identified a slower (group-I, red) and faster dynamical process (group-II, blue). **(b)** For the three mutants, ¹⁵N CPMG dispersion profiles for a representative residue in fast exchange (Gly74) from group II and slow exchange (Asn102) from group I¹¹. The fast-exchange process is virtually unaltered by the mutations, whereas R_{ex} increases consecutively from single via double to triple mutant (see also Supplementary Data 3). **(c, e, g)** Quantitative analysis of fast and slow protein dynamics of CypA rescue mutants by CPMG relaxation and CEST experiments are plotted onto the structure. Blue and red color coding of the cartoon representation denotes fast and slow dynamics as determined from the temperature-dependence and shape of CPMG relaxation dispersion profiles (Supplementary Data 1 and 2). Spheres represent residues in slow exchange with quantifiable CEST profiles. **(c)** CEST data for all 15 residues (red spheres) in S99T can be globally fit to a two-site exchange

134

process (Extended Data Fig. 3 and Supplementary Data 4). **(e, g)** Residues with CEST profiles in S99T/C115S (**e**) and S99T/C115S/I97V (**g**) are well-described by two distinct slow processes (red and green, respectively), whereas residues shown in orange sense both processes and require a three-site exchange model (Extended Data Figs. 4 and 5 and Supplementary Data 5 and 6). **(d, f, h)** Representative ¹⁵N CEST profiles of residue N102, measured at the indicated field strengths are shown for single (**d**), double (**f**), and triple (**h**) mutants of CypA. The chemical shifts for the major (solid line) and minor states (--- and - · - lines) are indicated. Uncertainties in $R_{2,\text{eff}}$ (panel b) are determined from the rmsd in the intensities of the duplicate points ($n = 4$) according to the definition of pooled relative standard deviation; uncertainties in I/I_0 for CEST data (panels d, f, h) are estimated from the scatter in the baseline of the profile (typically, $n > 50$).

145

146 For a quantitative understanding of the mechanism underlying the increased catalysis along the
147 directed evolution trajectory, we applied a powerful NMR method for studying systems in slow
148 exchange, chemical exchange saturation transfer (CEST) spectroscopy²⁰. The ¹⁵N-CEST
149 experiments identified a large number of residues in slow exchange in all mutant forms of CypA
150 (Fig. 2c-h; Extended Data Figs. 3-5 and Supplementary Data 4-6) and delivered two key results.
151 First, for the rescue mutants we observe two distinct slow dynamic clusters that differ in kinetics
152 and populations (Fig. 2e,g and Extended Data Figs. 4 and 5). The exchange profiles of 46 residues
153 for the double-, and 55 residues for the triple-mutant were globally fit to a linear, three-state
154 exchange model (see Online Methods). Second, we discover a gradual increase in the
155 interconversion rate from the major to the minor conformation for the slow process centered
156 around group-I residues ($k_{\text{maj} \rightarrow \text{min}} 2.3 \pm 0.1 \text{ s}^{-1}$ for S99T, $8.2 \pm 0.4 \text{ s}^{-1}$ for S99T/C115S and $11.5 \pm$
157 0.5 s^{-1} for S99T/C115S/I97V, respectively).

158

159 NMR relaxation experiments enable us to “see” the prevalence of exchange on different time scales
160 and to unravel their importance in biological processes⁴. The remarkable correspondence between
161 $k_{\text{maj} \rightarrow \text{min}}$ and k_{cat}/K_M (Fig. 3a) corroborates our hypothesis that the increased dynamics of group-I
162 residues is indeed responsible for the rescue in enzymatic activity. The good correlation between
163 the chemical shift differences, $\Delta\delta_{AB}$ and $\Delta\delta_{AC}$, in the two rescue mutants (Fig. 3b) indicates that
164 the exchange processes are the same by nature. The newly identified second slow exchange process
165 is located on the opposite side of the protein and partially overlaps with the faster loop motion
166 detected by CPMG experiments (Fig. 2e,g). The rather large chemical shift differences observed
167 for this exchange process (Fig. 3b, green squares) agree well with the predicted values of going to

168 a more extended/unfolded state (Extended Data Fig. 6) and are, therefore, unlikely to be relevant
169 for catalysis.

170

171 Since overall turnover in WT is dictated by $k_{\text{maj} \rightarrow \text{min}}$ and occurs on similar timescales in both the
172 apo enzyme and during turnover¹⁰, we needed to confirm that such a correspondence between the
173 measured dynamics in the apo and turnover protein holds true for the mutants. Therefore, CPMG
174 and CEST experiments were performed on S99T during enzymatic turnover of a substrate peptide.
175 These experiments on the mutants proved to be difficult and only possible for S99T due to stability,
176 and the weak affinity for the peptides allowed for a maximum of ~70% saturation. For S99T during
177 catalysis, we indeed observe both fast loop movement, and slow conformational dynamics in the
178 group-I residues, very similar to the apo protein (Fig. 3c-e). Together these data show that the
179 intrinsic dynamics in the group-I residues in the mutants are rate-limiting for the catalytic cycle.

180

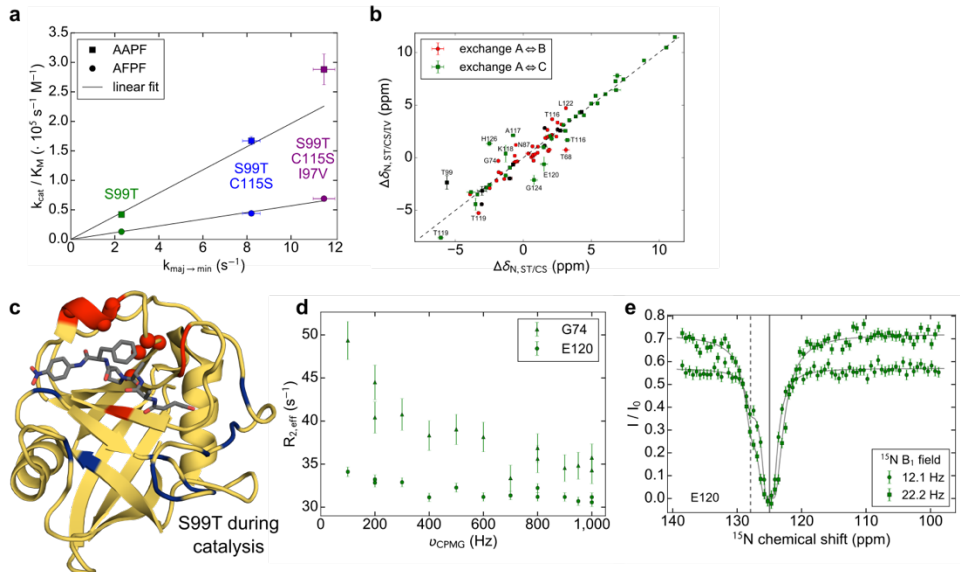


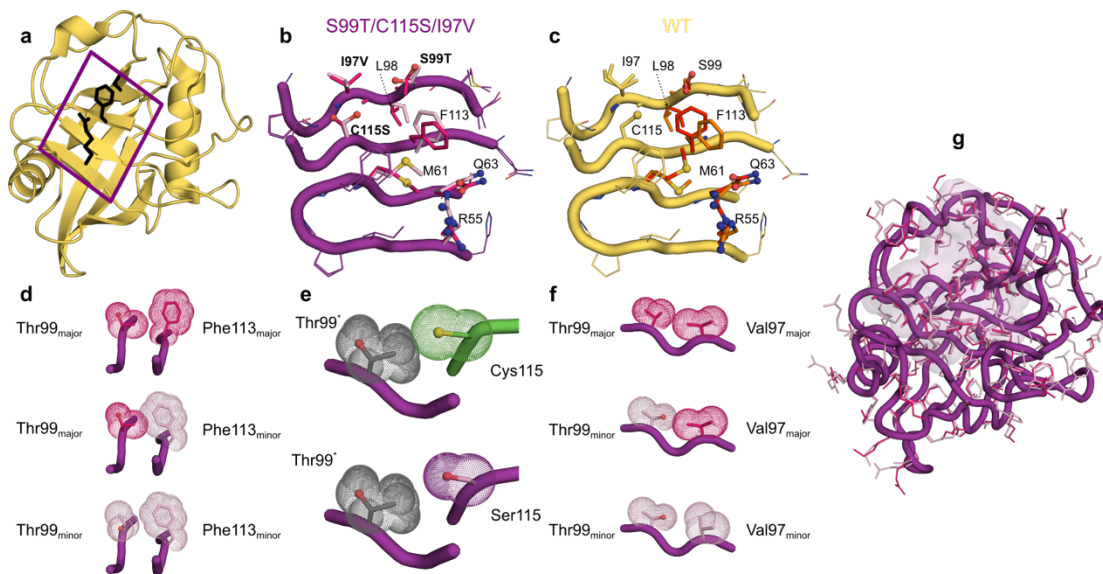
Figure 3 | Protein dynamics during turnover and catalytic efficiency correlate.

(a) Correlation between k_{cat}/K_M and $k_{\text{maj} \rightarrow \text{min}}$ measured by CEST across all rescue mutations for apo protein. (b) Correlation of the chemical shift differences between major and minor conformations for the two processes observed in S99T/C115S and S99T/C115S/I97V. Residues within 5 Å of mutation site (I97V) are shown in black and assignments are given if the variation in $\Delta\delta$ is >1.5 ppm. (c) Quantitative analysis of fast and slow protein dynamics of CypA S99T during catalysis of Suc-AFPP-pNA peptide (grey sticks) measured by NMR. CPMG relaxation dispersion experiments revealed, similarly as in apo S99T, fast motion mainly in the flexible loop (blue) and a slow process (red) consistent with the CEST data (spheres). (d) Representative CPMG profiles for a residue in fast (Gly74) and slow (Glu120) exchange and (e) CEST profile for Glu120 during catalysis (see Supplementary Data 7 and 8 for all profiles). Error bars in panels a and b denote the (propagated) standard errors in the fitted parameters. The uncertainties in CPMG (d) and CEST (e) data are determined as described in Fig. 2.

181
182
183
184
185
186
187
188
189
190
191
192
193
194
195
196

197 To reveal the structural basis of the increased dynamics in the group-I residues and hence increased
198 catalysis along the evolutionary trajectory, we collected room-temperature X-ray data for
199 S99T/C115S/I97V (Fig. 4). Alternate conformations were identified using qFit²¹ and the final
200 multiconformer model was obtained after subsequent manual adjustments and occupancy
201 refinement (Extended Data Fig. 7). A swap of the major/minor states from WT to
202 S99T/C115S/I97V is observed for the group-I residues, thereby directly delivering the atomic
203 structures of the conformations for which we measured their interconversion rate by NMR. Both
204 the C115S and I97V mutations subtly reduce the amino acid size, and combined partially restore

205 the “Phe113-in” conformation as a minor conformation that can now be directly observed in the
 206 electron density (Fig. 4b,d-f). The interpretation of increased conformational heterogeneity of
 207 Phe113 and Thr99 was additionally confirmed by an alternative ensemble refinement method
 208 (Extended Data Fig. 8). The size reduction by the C115S mutation could contribute to the faster
 209 transition between the major and minor conformation due to the relief of a clash between the larger
 210 sulfur atom and Thr99 (Fig. 4e).



211
 212
213 Figure 4 | Structural basis of the increased protein dynamics from room-temperature X-ray
214 crystallography on rescue mutants.

215 (a) X-ray structure of CypA (2CPL³⁰) with the active-site residues Arg55, Ser99 and Phe113
 216 shown in black stick representation. The boxed area indicates the extended dynamic network
 217 shown in more detail in b-c. (b) Major and minor side chain conformations are shown for
 218 S99T/C115S/I97V (5WC7, 1.43 Å, see Extended Data Table 1) in purple and pink, respectively.
 219 The populations are flipped relative to wild-type CypA (3K0N, 1.4 Å)¹¹ (c), where major/minor
 220 states are shown in red and orange, respectively. (e, f, g) Less steric hindrance due to the reduced
 221 size of side chains in rescue mutants facilitates the interconversion between major and minor
 222 conformations. Coupling between the conformation of Thr99 and Phe113 (e) and Val97 and Thr99
 223 (g) are necessary to relieve clashes. (f) The C115S (purple) mutation allows for a transition
 224 between Thr99 conformations (grey indicates morph between the major and minor state labeled
 225 Thr99*) without clash, in contrast to the bulkier Cys residue (green). (h) CONTACT analysis²² of
 226 alternative conformations of S99T/C115S/I97V identifies a network extending across group-I
 227 residues (pink surface representation) consistent with the NMR results.

228

229 The connection between these alternate conformations and the collective fitting of the NMR
230 dynamics is further buttressed by analysis of contacts between alternative conformations²², which
231 identifies a network across the protein that coincides with the group-I residues (Fig. 4g). While the
232 detection of alternate conformations by X-ray diffraction does not per se deliver information about
233 correlated motions, a detailed analysis of the steric constraints of group-I residues (Fig. 4d-f)
234 exposes how motions from the active site are propagated in a correlated manner. These structural
235 results, together with the characterization of collective dynamics by NMR, reveal how the
236 mutations selected by directed evolution have rewired the internal packing to increase the
237 dynamics of Phe113 correlated with surrounding group-I residues during the catalytic cycle.

238

239 Why did additional rounds of directed evolution fail to yield further improvement in the catalytic
240 rate? We speculate that the enzyme may be in a local minimum in the fitness landscape, and that
241 a specific combination of mutations is needed for further improvement, including mutations that
242 are neutral or mildly deleterious mutations on their own, in agreement with the dominance of
243 epistasis in protein evolution²³.

244

245 Characterizing how directed evolution shaped the energy landscape for enhanced catalytic activity
246 by solely increasing the conformational interconversion rates in a specific dynamic network has
247 broad implications for resolving controversies about the role of protein dynamics in enzyme
248 catalysis of modern enzymes, and in discovering the mechanism of improved catalysis via directed
249 evolution. We briefly discuss both points in respect to pertinent current views in these fields.
250 Fueled by a strong dispute about protein dynamics impact on catalysis^{24,25}, the field has focused
251 on characterizing several enzymes mechanistically in great detail using a combination of

252 experimental and computational approaches, including CypA^{9-11,19,26}. A two-state ensemble
253 calculation using exact NOEs as constraints revealed an open- and closed-state of free CypA with
254 respect to the position of the 64-74 loop¹⁹. The authors postulate that this loop dynamics is directly
255 linked to catalysis via long-range concerted motions extending to the active site. This model is
256 incompatible with the loop dynamics measured here, which remains fast for all CypA forms and
257 is not correlated to catalytic turnover. In contrast, the group-I residues could be directly linked to
258 catalysis via concurring changes in dynamics between WT, S99T, and the evolved enzyme forms,
259 and catalytic turnover rates. This highlights the importance of NMR dynamics measurements and
260 their quantitative comparison to corresponding changes in catalytic rates, which cannot be
261 extracted from an ensemble-averaged NOE-based structure calculation.

262 The slowness of conformational interconversion in CypA requires enhanced computational
263 sampling methods for MD simulations. Transitions between the experimentally determined
264 conformational states¹¹ were calculated using parallel-tempering metadynamics resulting in a free
265 energy difference for S99T²⁷ that is in excellent agreement with the experimental value of -2.5
266 kcal/mol obtained here from the CEST data. A two-state ensemble for the cis- and trans-peptide
267 bound CypA calculated by replica-exchange MD simulations in combination with NMR
268 constraints²⁶ show only minimal protein conformational differences compared to the starting
269 crystal structures (Extended Data Fig. 9). This is in sharp contrast to our NMR dynamics for WT¹⁰
270 and S99T during catalysis measured here, which clearly shows that conformational sub-states
271 interconvert across the core catalytic network and that this rate is correlated to catalysis.

272

273 It is notable that the function of CypA was modulated by mutations that do not directly contact the
274 substrate. While the results of numerous “second shell” mutations emerging from directed

275 evolution experiments have been interpreted based on speculative links between protein dynamics
276 and changes in activity, experimental evidence of alterations of populations or kinetics of
277 alternative conformations has been sparse¹³. Here, the increased dynamics can be rationalized by
278 the ability of Phe113, which directly abuts the substrate, to transition between different rotameric
279 states. This transition is controlled by the repacking of alternative conformations of core residues,
280 such as Thr99, and is enabled by the decreased bulk of the mutated residues (Cys>Ser; Ile>Val).
281 NMR spectroscopy directly reveals how the kinetics of these transitions between alternative
282 internal packing arrangements controls the increased catalytic activity accumulated during directed
283 evolution. The slow dynamics associated with the catalytic cycle of CypA, and likely for many
284 other enzymes, are only now becoming accessible to molecular simulations²⁸. Therefore, the
285 lessons of how non-active site mutations can alter conformational dynamics, derived from our
286 integrated analysis of room-temperature X-ray data and NMR dynamics measurements, could be
287 applied more broadly to aid the long-term goal of rationally improving directed evolution.

288

289 **References:**

290

- 291 1 Blomberg, R. *et al.* Precision is essential for efficient catalysis in an evolved Kemp
292 eliminase. *Nature* **503**, 418-421, doi:10.1038/nature12623 (2013).
- 293 2 Romero, P. A. & Arnold, F. H. Exploring protein fitness landscapes by directed evolution.
294 *Nat Rev Mol Cell Biol* **10**, 866-876, doi:10.1038/nrm2805 (2009).
- 295 3 Arnold, F. H. The nature of chemical innovation: new enzymes by evolution. *Q Rev
296 Biophys* **48**, 404-410, doi:10.1017/S003358351500013X (2015).
- 297 4 Kay, L. E. New Views of Functionally Dynamic Proteins by Solution NMR Spectroscopy.
298 *J Mol Biol* **428**, 323-331, doi:10.1016/j.jmb.2015.11.028 (2016).

- 299 5 Boehr, D. D., Dyson, H. J. & Wright, P. E. An NMR perspective on enzyme dynamics.
- 300 *Chem Rev* **106**, 3055-3079, doi:10.1021/cr050312q (2006).
- 301 6 Smock, R. G. & Giersch, L. M. Sending signals dynamically. *Science* **324**, 198-203,
- 302 doi:10.1126/science.1169377 (2009).
- 303 7 Palmer, A. G., 3rd. Enzyme dynamics from NMR spectroscopy. *Acc Chem Res* **48**, 457-
- 304 465, doi:10.1021/ar500340a (2015).
- 305 8 Shukla, D., Hernandez, C. X., Weber, J. K. & Pande, V. S. Markov state models provide
- 306 insights into dynamic modulation of protein function. *Acc Chem Res* **48**, 414-422,
- 307 doi:10.1021/ar5002999 (2015).
- 308 9 Eisenmesser, E. Z., Bosco, D. A., Akke, M. & Kern, D. Enzyme dynamics during
- 309 catalysis. *Science* **295**, 1520-1523, doi:10.1126/science.1066176 (2002).
- 310 10 Eisenmesser, E. Z. *et al.* Intrinsic dynamics of an enzyme underlies catalysis. *Nature*
- 311 **438**, 117-121, doi:10.1038/nature04105 (2005).
- 312 11 Fraser, J. S. *et al.* Hidden alternative structures of proline isomerase essential for
- 313 catalysis. *Nature* **462**, 669-673, doi:10.1038/nature08615 (2009).
- 314 12 Harms, M. J. & Thornton, J. W. Evolutionary biochemistry: revealing the historical and
- 315 physical causes of protein properties. *Nat Rev Genet* **14**, 559-571, doi:10.1038/nrg3540
- 316 (2013).
- 317 13 Ma, B. & Nussinov, R. Protein dynamics: Conformational footprints. *Nat Chem Biol* **12**,
- 318 890-891, doi:10.1038/nchembio.2212 (2016).
- 319 14 Kern, D., Kern, G., Scherer, G., Fischer, G. & Drakenberg, T. Kinetic analysis of
- 320 cyclophilin-catalyzed prolyl cis/trans isomerization by dynamic NMR spectroscopy.
- 321 *Biochemistry* **34**, 13594-13602 (1995).
- 322 15 Harrison, R. K. & Stein, R. L. Mechanistic studies of peptidyl prolyl cis-trans isomerase:
- 323 evidence for catalysis by distortion. *Biochemistry* **29**, 1684-1689 (1990).

- 324 16 Coaker, G., Zhu, G., Ding, Z., Van Doren, S. R. & Staskawicz, B. Eukaryotic cyclophilin
325 as a molecular switch for effector activation. *Mol Microbiol* **61**, 1485-1496,
326 doi:10.1111/j.1365-2958.2006.05335.x (2006).
- 327 17 Aumuller, T., Jahreis, G., Fischer, G. & Schiene-Fischer, C. Role of prolyl cis/trans
328 isomers in cyclophilin-assisted *Pseudomonas syringae* AvrRpt2 protease activation.
329 *Biochemistry* **49**, 1042-1052, doi:10.1021/bi901813e (2010).
- 330 18 Kofron, J. L., Kuzmic, P., Kishore, V., Colon-Bonilla, E. & Rich, D. H. Determination of
331 kinetic constants for peptidyl prolyl cis-trans isomerases by an improved
332 spectrophotometric assay. *Biochemistry* **30**, 6127-6134 (1991).
- 333 19 Chi, C. N. et al. A Structural Ensemble for the Enzyme Cyclophilin Reveals an
334 Orchestrated Mode of Action at Atomic Resolution. *Angew Chem Int Ed Engl* **54**, 11657-
335 11661, doi:10.1002/anie.201503698 (2015).
- 336 20 Vallurupalli, P., Bouvignies, G. & Kay, L. E. Studying "invisible" excited protein states in
337 slow exchange with a major state conformation. *J Am Chem Soc* **134**, 8148-8161,
338 doi:10.1021/ja3001419 (2012).
- 339 21 Keedy, D. A., Fraser, J. S. & van den Bedem, H. Exposing Hidden Alternative Backbone
340 Conformations in X-ray Crystallography Using qFit. *PLoS Comput Biol* **11**, e1004507,
341 doi:10.1371/journal.pcbi.1004507 (2015).
- 342 22 van den Bedem, H., Bhabha, G., Yang, K., Wright, P. E. & Fraser, J. S. Automated
343 identification of functional dynamic contact networks from X-ray crystallography. *Nat
344 Methods* **10**, 896-902, doi:10.1038/nmeth.2592 (2013).
- 345 23 Tokuriki, N. et al. Diminishing returns and tradeoffs constrain the laboratory optimization
346 of an enzyme. *Nat Commun* **3**, 1257, doi:10.1038/ncomms2246 (2012).
- 347 24 Nagel, Z. D. & Klinman, J. P. A 21st century revisionist's view at a turning point in
348 enzymology. *Nat Chem Biol* **5**, 543-550, doi:10.1038/nchembio.204 (2009).

349 25 Kamerlin, S. C. & Warshel, A. At the dawn of the 21st century: Is dynamics the missing
350 link for understanding enzyme catalysis? *Proteins* **78**, 1339-1375,
351 doi:10.1002/prot.22654 (2010).

352 26 Camilloni, C. *et al.* Cyclophilin A catalyzes proline isomerization by an electrostatic
353 handle mechanism. *Proc Natl Acad Sci U S A* **111**, 10203-10208,
354 doi:10.1073/pnas.1404220111 (2014).

355 27 Papaleo, E., Sutto, L., Gervasio, F. L. & Lindorff-Larsen, K. Conformational Changes
356 and Free Energies in a Proline Isomerase. *J Chem Theory Comput* **10**, 4169-4174,
357 doi:10.1021/ct500536r (2014).

358 28 Dodani, S. C. *et al.* Discovery of a regioselectivity switch in nitrating P450s guided by
359 molecular dynamics simulations and Markov models. *Nat Chem* **8**, 419-425,
360 doi:10.1038/nchem.2474 (2016).

361 29 Zhao, Y. & Ke, H. Crystal structure implies that cyclophilin predominantly catalyzes the
362 trans to cis isomerization. *Biochemistry* **35**, 7356-7361, doi:10.1021/bi9602775 (1996).

363 30 Ke, H. Similarities and differences between human cyclophilin A and other β -barrel
364 structures. *Journal of Molecular Biology* **228**, 539-550, doi:10.1016/0022-
365 2836(92)90841-7 (1992).

366

367

368 **Methods**

369

370 **Library Screen.** Mutant libraries were created using error prone PCR as in Rockah-Shmuel *et*
371 *al.*³¹. For the initial library used to isolate S99T/C115S and subsequent screening efforts, the
372 mutation rate was tuned to <3 new mutations per gene. Over 1,000 individual clones were screened
373 in the initial screen that identified S99T/C115S and an additional 1,500 clones were screened in a

374 second library to identify S99T/C115S/I97V. Subsequent screens of more than 5,000 variants,
375 including random mutations and focused libraries randomizing contacting residues, to identify
376 additional mutations did not yield any new mutations with gains of function.

377 From transformations of >10,000 individual colonies, individual isolates were picked into
378 96 well blocks and grown overnight at 37 °C. For induction, 4 µl of the overnight culture was
379 diluted into a fresh 96 well block containing 1 mL of LB and grown for 3 hours prior to addition
380 of 100 µM IPTG. The induced culture was then grown overnight at room temperature and
381 harvested by centrifugation at 3000xg for 15 minutes. The media was decanted from the 96 well
382 block and 125 µL of lysis buffer (20 mM Tris, pH 8.0, 1% Triton S100) was added. The block was
383 shaken for 30 minutes at room temperature and then frozen at -80 °C.

384 Prior to assaying the AvrRpt2 activity, the 96 well block was thawed. To remove the
385 membrane and unlysed cells, the thawed lysate was centrifuged at 3000xg for 15 minutes. 30 µL
386 of the extract was transferred carefully to a 96 well plate. A master mix of inactive 0.25 mg/mL
387 AvrRpt2 and 1 mM substrate peptide (Abz-IEAPAFGGWy-NH₂, where y = 3-nitro-Tyrosine)
388 were mixed in reaction buffer (20 mM HEPES, pH 8.5, 50 mM NaCl, 1 mM DTT). The reaction
389 was initiated by mixing 10 µL of lysate with 30 µL of master mix in a Costar Black Flat bottom
390 96 well plate (Corning, product #3694) and measured in a Safire microplate reader monitoring
391 fluorescence at 418 nm (excitation at 340 nm).

392

393 **Sample Preparation.** Wild-type CypA and mutant proteins were essentially expressed and
394 purified as described previously⁹. Briefly, LB medium or M9 minimal medium containing 2 g/L
395 U-[¹³C]-D-glucose and/or 1 g/L ¹⁵NH₄Cl (Cambridge Isotope Laboratories, Tewksbury, MA,
396 USA) as the sole carbon and nitrogen source were used to express unlabeled and ¹³C/¹⁵N-labeled

397 or ^{15}N -labeled CypA, respectively. Cells were grown at 37 °C to an OD₆₀₀ ~0.6 after which protein
398 expression was induced with 0.3 mM IPTG for 4 hours at the same temperature (wild-type and
399 S99T) or overnight at 20 °C (S99T/C115S and S99T/C115S/I97V). Cells were lysed in 25 mM
400 MES, pH 6.1, 5 mM β -mercaptoethanol and purified on a SP-Sepharose column using a NaCl
401 gradient. Fractions containing CypA were pooled and dialysed overnight into 50 mM Na₂HPO₄,
402 pH 6.8, 5 mM β -mercaptoethanol. Remaining DNA and other impurities were removed using a Q-
403 Sepharose column by collecting the flow-through. CypA was purified to homogeneity on a size-
404 exclusion column (HiLoad 16/600, S75) equilibrated in 50 mM Na₂HPO₄, pH 6.5, 250 mM NaCl,
405 5 mM β -mercaptoethanol. Samples were dialysed overnight into their final buffers (50 mM
406 Na₂HPO₄, pH 6.5, 1 mM TCEP for NMR and 20 mM HEPES, pH 7.5, 100 mM NaCl, 0.5 mM
407 TCEP for activity measurements, respectively). All purification steps were performed at 4 °C.
408

409 **Crystallography.** S99T/C115S/I97V CypA was produced and crystallized similarly to previous
410 studies of wild-type CypA¹¹. Briefly, crystals were grown by mixing equal volumes of well
411 solution (100 mM (4-(2-hydroxyethyl)-1-piperazineethanesulfonic acid) HEPES, pH 7.5, 23%
412 PEG 3350, 5 mM Tris (2-carboxymethyl) phosphine [TCEP]) and protein (60 mg/mL in 20 mM
413 HEPES, pH 7.5, 100 mM NaCl, 0.5 mM TCEP) in the hanging-drop format. To collect the room-
414 temperature synchrotron dataset, paratone oil was applied to cover a 2 μL hanging drop containing
415 a single large crystal of S99T/C115S/I97V CypA. The crystal was harvested through the paratone
416 and excess mother liquor was removed using a fine paper wick. Attenuated data were collected at
417 ALS beamline 8.3.1 with a collection wavelength of 1.115 Å at 273 K controlled by the cryojet
418 using an ADSC Q315r detector. Data were processed using XDS³², monitoring scaling statistics

419 to confirm a lack of radiation damage³³ and CC statistics for high resolution cutoffs³⁴, to 1.43 Å
420 resolution.

421 Molecular replacement was performed in Phaser³⁵ using 2CPL³⁰ as an initial search model.
422 Residues were manually mutated in Coot³⁶ and subjected to multiple rounds of refinement using
423 phenix.refine³⁷. To add alternative conformations in a systematic manner, the refined single
424 conformer model was rebuilt using qFit²¹. To finalize the model, further manual improvements to
425 the connectivity of alternative conformations and the ordered solvent molecules were performed
426 iteratively with cycles of phenix.refine. Structure validation was performed using MolProbity and
427 yielded the following statistics for Ramachandran (favored: 96%, allowed 4%, outliers: 0%), 1.4%
428 rotamer outliers and a clashscore of 0.98.

429 Analysis of contacting residues using CONTACT was performed (parameters: T_{stress} 0.35
430 and Relief 0.9), as for wild-type CypA²². Ensemble refinements were performed using
431 phenix.ensemble_refinement³⁸. All figures were prepared using PyMol³⁹.

432 **Enzyme activity.** k_{cat}/K_M for the enzyme catalyzed *cis*-to-*trans* isomerization of succinyl-AAPF-
433 p-nitroanilide and succinyl-AAPF-p-nitroanilide (Suc-AXPF-pNA; Bachem) was measured at
434 10 °C using the standard chymotrypsin-coupled assay¹⁸. The increase in absorbance at 390 nm was
435 fit to a single exponential to yield a rate constant for the interconversion between *cis*- and *trans*-
436 peptide. Both the uncatalyzed, background (triplicates) and enzyme-catalyzed reaction were
437 (average/standard deviation of at least three different enzyme concentrations, each measured in
438 triplicate) measured for both peptides and different enzyme concentrations chosen such that the
439 rate of the enzyme-catalyzed reaction is between 3- and 15-fold faster than the uncatalyzed
440 reaction.

441

442 **NMR spectroscopy and data analysis.** NMR experiments were recorded on an Agilent DD2 600
443 MHz four-channel spectrometer equipped with a triple-resonance cryogenically cooled probe-head
444 or a Varian Unity Inova 500 MHz spectrometer equipped with a room-temperature triple-
445 resonance probe. NMR samples contained 0.25 mM (for peptide K_D experiments) or 1 mM (all
446 other experiments) CypA in 50 mM Na₂HPO₄, pH 6.5, 1 mM TCEP, 0.02% NaN₃ and 10 (v/v) %
447 D₂O. The CypA S99T + AFPF sample contained ~0.85 mM CypA and 10.5 mM Suc-AFPF-pNA.
448 Sample temperatures were calibrated using the 4% methanol + 96% methanol-d₄ sample (DLM-
449 5007, Cambridge Isotope Laboratories).

450 All data sets were processed with the NMRPipe/NMRDraw software package⁴⁰ and
451 visualized/analysed using the program NMRFAM-SPARKY⁴¹.

452

453 **Backbone assignments.** TROSY-versions of a 3D HNCACB⁴² and CBCA(CO)NH⁴³ experiments
454 were recorded at 25 °C to obtain a nearly complete sequential backbone resonance assignment
455 (H^N, N, C^α, C^β) of CypA S99T/C115 and S99T/C115S/I97V. The HNCACB experiments were
456 acquired with 50 (¹⁵N) × 70 (¹³C) × 537 (¹H) complex points, with maximum evolution times equal
457 to 22.2 (¹⁵N) × 8.3 (¹³C) × 64.0 (¹H) ms. An interscan delay of 1 s was used with 8 scans per
458 transient, giving rise to a net acquisition time of 36 h. The CBCA(CO)NH experiments were
459 acquired with 59 (¹⁵N) × 50 (¹³C) × 537 (¹H) complex points, with maximum evolution times equal
460 to 26.2 (¹⁵N) × 5.9 (¹³C) × 64.0 (¹H) ms. An interscan delay of 1 s was used with 8 scans per
461 transient, giving rise to a net acquisition time of 30 h. Cross peak assignments were propagated to
462 CPMG and CEST experiments at lower temperatures using [¹H-¹⁵N]-TROSY-HSQC^{44,45} spectra
463 recorded at different temperatures between 10 and 25 °C and where necessary confirmed using a
464 3D ¹⁵N-edited NOESY⁴⁶ data set recorded at 10 °C. Cross peaks for Val2 and Glu81 were not

465 visible at 25 °C, but could be assigned from the data recorded at 10 °C. The chemical shift
466 assignments of CypA S99T/C115S and S99T/C115S/I97V have been deposited in the
467 BioMagResBank⁴⁷ with accession codes 27217 and 27218, respectively.

468

469 **K_D measurements.** Dissociation constants for Suc-AFPF-pNA at 10 °C were obtained by titrating
470 the peptide (final concentrations: 0, 1, 3, 5, 9 mM) into a solution of 0.25 mM CypA. Line-shape
471 fitting was performed using PINT⁴⁸ to obtain cross peak positions in the individual spectra. The
472 combined chemical shift difference Δδ was calculated according to:

473
$$\Delta\delta \text{ (ppm)} = [\Delta\delta_H^2 + (\Delta\delta_N / R_{\text{scale}})^2]^{1/2},$$

474 where $R_{\text{scale}} = 6.3$ was determined according to Mulder *et al.*⁴⁹. Resonances with sufficient signal-
475 to-noise and for which $\Delta\delta \geq 0.035$ ppm were included in the fits to determine dissociation constants
476 using the following equation:

477

478
$$\Delta\delta = \Delta\delta_{\text{sat-apo}} \cdot \frac{([AFPF] + [CypA] + K_D) - \sqrt{([AFPF] + [CypA] + K_D)^2 - 4 \cdot [AFPF] \cdot [CypA]}}{2 \cdot [CypA]}$$

479

480 where [CypA] is the total enzyme concentration, [AFPF] is the concentration of peptide and $\Delta\delta_{\text{sat-}}$
481 $_{\text{apo}}$ is the combined chemical shift difference between apo and saturated CypA.

482 All resonances (13, 23, and 26 for CypA S99T, S99T/C115S and S99T/C115S/I97V,
483 respectively) were fit simultaneously in Mathematica 11⁵⁰ and standard errors are obtained from
484 the global fit. The solubility of the peptide and sample stability limits the highest achievable
485 concentration in our titration experiments and we could only attain data up to 5 mM AFPF for the
486 double- and triple-mutant.

487

488 **CPMG relaxation dispersion experiments.** Relaxation dispersion experiments on CypA were
489 recorded on a 600 MHz spectrometer at different temperatures (10 and 15 °C for all mutants, and
490 additionally at 20 °C for the triple-mutant). A TROSY-version of the relaxation-compensated ¹⁵N-
491 CPMG pulse sequence^{51,52} was used, with the CPMG period implemented in a constant-time
492 manner⁵³.

493 The experiments were recorded as a series of 16 interleaved 2D data sets, with the constant-
494 time relax period set to 40 ms. The CPMG field strengths were equal to 100, 200, 300, 400, 500,
495 600, 700, 800, 900, 950, and 1000 Hz, with duplicate experiments recorded for the reference
496 experiment and 200, 800 and 1000 Hz. Experiments were acquired with $128 - 155$ (¹⁵N) $\times 536$
497 (¹H) complex points, with maximum evolution times equal to $56.9 - 68.9$ (¹⁵N) $\times 63.9$ (¹H) ms.
498 An interscan delay of 2 s was used with 16, 24, or 32 scans per transient, giving rise to net
499 acquisition times between 40 – 88 h for a complete pseudo-3D data set.

500 Line-shape fitting was performed using PINT⁴⁸ and the obtained cross peak volumes were
501 used to calculate the values of $R_{2,\text{eff}}$. Error estimation in the experimental data using the four
502 duplicate data points was performed as described earlier by Mulder *et al.*⁵⁴. For ease of comparison,
503 the values of $R_{2,\text{inf}}$ were calculated by taking the average of the $R_{2,\text{eff}}$ at the three highest v_{CPMG}
504 values (i.e., 900, 950 and 1000 Hz) and normalized to the lowest temperature.

505

506 **CEST experiments.** ¹⁵N-CEST experiments²⁰ on CypA were recorded on a 500 MHz
507 spectrometer at 10 °C for two (single- and triple-mutants) or three (double-mutant) different ¹⁵N
508 B_1 field strengths. The weak irradiation fields applied during the relaxation delay were calibrated
509 from 1D spectra as described by Guenneugues *et al.*⁵⁵ with the irradiation position set to an isolated
510 cross peak that did not show exchange.

511 The experiments on CypA S99T were recorded with a ^1H decoupling field strength of 2.3
512 kHz (using $90_x240_y90_x$ composite pulses) during the relaxation delay, T_{EX} , of 0.5 s. Two different
513 ^{15}N B_1 fields, 16.3 and 29.7 Hz, were used and a series of 2D data sets were acquired with ^{15}N
514 offsets ranging between 96.5 (97.7) and 140.4 (139.2) ppm, in 112 (85) increments of 20 (25) Hz
515 for $v_1 = 16.3$ Hz ($v_1 = 29.7$ Hz), and one reference experiment. Each 2D data set comprised of 110
516 (^{15}N) \times 512 (^1H) complex points, with maximum evolution times equal to 52.4 (^{15}N) \times 64 (^1H) ms,
517 an interscan delay of 1.5 s and eight scans per transient were used, giving rise to net acquisition
518 times of about 118 h ($v_1 = 16.3$ Hz) and 94 h ($v_1 = 29.7$ Hz).

519 For CypA S99T in the presence of Suc-AFPF-pNA, two different ^{15}N B_1 fields, 12.1 and
520 22.2 Hz, were used and a series of 2D data sets were acquired with ^{15}N offsets ranging between
521 98.7 and 138.5 ppm, in 73 increments of 28 Hz, and one reference experiment. The experiments
522 were recorded with a ^1H decoupling field strength of 2.25 kHz (using $90_x240_y90_x$ composite
523 pulses) during the relaxation delay, T_{EX} , of 0.4 s ($v_1 = 22.2$ Hz) or 0.5 s ($v_1 = 12.1$ Hz). Each 2D
524 data set comprised of 110 (^{15}N) \times 512 (^1H) complex points, with maximum evolution times equal
525 to 52.4 (^{15}N) \times 64 (^1H) ms, an interscan delay of 1.5 s and twelve scans per transient were used,
526 giving rise to net acquisition times of about 112 h ($v_1 = 22.2$ Hz) and 116 h ($v_1 = 12.1$ Hz).

527 For CypA S99T/C115S, three different ^{15}N B_1 fields, 12.2, 23.6, and 34.7 Hz, were used
528 and a series of 2D data sets were acquired with ^{15}N offsets ranging between 97.8 and 139.2 ppm,
529 in 106 increments of 20 Hz, and one reference experiment. The experiments were recorded with a
530 ^1H decoupling field strength of 2.3–2.4 kHz (using $90_x240_y90_x$ composite pulses) during the
531 relaxation delay, T_{EX} , of 0.4 s ($v_1 = 23.6$ Hz) or 0.5 s ($v_1 = 12.2$ and 23.6 Hz). Each 2D data set
532 comprised of 110 (^{15}N) \times 512 (^1H) complex points, with maximum evolution times equal to 52.4

533 (^{15}N) \times 64 (^1H) ms, an interscan delay of 1.5 s and eight scans per transient were used, giving rise
534 to net acquisition times of about 107 h ($v_1 = 23.6$ Hz) and 112 h ($v_1 = 12.2$ and 23.6 Hz).

535 The experiments on CypA S99T/C115S/I97V were recorded with a ^1H decoupling field
536 strength of 2.4 kHz (using $90_x 240_y 90_x$ composite pulses) during the relaxation delay, T_{EX} , of 0.4
537 s. Two different ^{15}N B_1 fields, 10.8 and 22.0 Hz, were used and a series of 2D data sets were
538 acquired with ^{15}N offsets ranging between 97.8 and 139.2 ppm, in 106 (85) increments of 20 (25)
539 Hz for $v_1 = 10.8$ Hz ($v_1 = 22.0$ Hz), and one reference experiment. Each 2D data set comprised of
540 110 (^{15}N) \times 512 (^1H) complex points, with maximum evolution times equal to 52.4 (^{15}N) \times 64 (^1H)
541 ms, an interscan delay of 1.5 s and eight scans per transient were used, giving rise to net acquisition
542 times of about 86 h ($v_1 = 22.0$ Hz) and 107 h ($v_1 = 10.8$ Hz).

543

544 **CEST data analysis.** Line-shape fitting was performed using PINT⁴⁸ and the obtained cross peak
545 volumes were used to calculate the ratio I / I_0 . The ^{15}N -CEST profiles (ratio versus irradiation
546 position) were analysed using the Python package ChemEx v0.6 (available from
547 <https://github.com/gbouvignies/chemex>), which numerically propagates the Bloch-McConnell
548 equations⁵⁶, as described earlier²⁰. Uncertainties in the ratio I / I_0 were estimated from the apparent
549 scatter in the baseline of the CEST profiles, whereas uncertainties in the fitting parameters (i.e.,
550 rate constants, populations and chemical shift differences) were determined from either the
551 covariance matrix or 400-500 Monte-Carlo runs.

552

553 We analysed all the CEST profiles assuming the absence of exchange, a two-site exchange model
554 and, if required, a three-site exchange model (only for CypA S99T/C115S and S99T/C115S/I97V).
555 In the “no-exchange” situation, the values of k_{ex} , p_B , $\Delta\omega$ and ΔR_2 were fixed at 0 and only R_1 , R_2

556 and I_0 were fit on a per-residue basis. Residues that showed elevated R_2 values and for which the
557 χ^2_{red} was significantly above 1, are likely candidates to experience an exchange process (Extended
558 Data Figs. 3b, 4f and 5f).

559
560 For the two-site exchange model, initially only residues that showed a clear second dip or
561 asymmetry were included. A per-residue fit was performed where in addition to the parameters
562 above also k_{ex} , p_B and $\Delta\omega$ were allowed to float.

563 The clustering of k_{ex}/p_B values for this initial subset indicated a single exchange process
564 for CypA S99T (Extended Data Fig. 3a), and a global fit was performed after updating the initial
565 k_{ex} , p_B and residue-specific $\Delta\omega$ values. As a third step, we fixed the global exchange parameters,
566 (k_{ex} and p_B) and re-fitted all residues. Residues that had a fitted value of $|\Delta\omega| \geq 1$ ppm, an improved
567 χ^2_{red} and consistent fitting parameters in Monte-Carlo runs (not fixing k_{ex} and p_B), were included
568 in the list of probes experiencing exchange. Finally, a global fit and 500 Monte-Carlo runs were
569 performed with every exchanging residue and now allowing all parameters [k_{ex}/p_B (global) and
570 $\Delta\omega$, R_1 , R_2 , ΔR_2 and I_0 (residue-specific)] to float. The results of this Monte-Carlo analysis are
571 shown in Extended Data Fig. 3c for k_{ex}/p_B and chemical shift differences are plotted on the
572 structure (Extended Data Fig. 3d). Furthermore, assuming a two-state exchange model, the χ^2_{red}
573 and fitted R_2 values for exchanging residues went down to their expected values, with the exception
574 of the loop region undergoing exchange on the millisecond timescale that still exhibits high R_2
575 values (Extended Data Fig. 3b).

576 On the contrary, for CypA S99T/C115S and S99T/C115S/I97V the clustering of k_{ex}/p_B
577 values for the initial subset suggested the presence of two different processes (Extended Data Figs.
578 4a and 5a). Residues that seemingly fitted well to a two-site exchange model were grouped into

579 two clusters and separately fitted to a global process, yielding two different rates of interconversion
580 and populations (Extended Data Figs. 4b and 5b). In a similar manner as for CypA S99T we
581 separately fixed the two combinations of global exchange parameters and re-fitted all data.
582 Residues that had a fitted value of $|\Delta\omega| \geq 1$ ppm, an improved χ^2_{red} and consistent fitting parameters
583 in Monte-Carlo runs (not fixing k_{ex} and p_B), were included in the appropriate cluster of probes
584 experiencing exchange. The two clusters were obtained consistently even when k_{ex}/p_B values from
585 the other one were used as starting points of the minimization. The residues present in the clusters
586 are found in two different parts of the protein (*cf.* green and red spheres in Fig. 2e,g) and also have
587 different R_{ex} contributions in the CPMG relaxation dispersion profiles (Supplementary Data 1 and
588 2). Furthermore, CEST data for several residues, including F88 and N102, could not be fit to a
589 two-site exchange model (Extended Data Figs. 4c and 5c).

590 Taken together, these observations show that the CEST data for the double- and triple-mutant
591 require a three-state exchange model to explain the data. We note that for some residues (*cf.* orange
592 spheres in Fig. 2e,g), the fast loop motion and slow processes give rise to convoluted exchange
593 data. However, this does not automatically mean that any (or all) of these processes are correlated;
594 it can simply be that a probe participating in one exchange process “feels” the fluctuating field of
595 another, nearby exchange phenomena.

596 There are several possibilities to connect three different states (A=ground state, B=minor
597 state 1, and C=minor state 2): one triangular model, where all states are connected, and three linear
598 models ($A \leftrightarrow B \leftrightarrow C$, $A \leftrightarrow C \leftrightarrow B$, and $B \leftrightarrow A \leftrightarrow C$) as described earlier by Sekhar *et al.*⁵⁷. We did not
599 consider the triangular model as it requires one additional fitting parameter and our NMR data is
600 not of high enough quality to warrant this. From fitting the individual residues, we already obtained
601 two values for $k_{\text{ex}}/\text{population}$ (Extended Data Figs. 4b and 5b) and $\Delta\omega$ values, and those were used

602 as starting values in the linear models. The combination with highest population was used as
603 $k_{ex,AB}/p_B/\Delta\omega_{AB}$ and the other as $k_{ex,AC}/p_C/\Delta\omega_{AC}$. The ACB-model, where the least populated minor
604 state is the intermediate, did not fit the data; whereas the other two models gave very similar results
605 and seem to describe the data equally well. Based on our current NMR and crystallography
606 experiments and earlier data on CypA S99T¹¹, we favor the $B \leftrightarrow A \leftrightarrow C$ model, where both
607 processes are independent and this model has been used for further analysis.

608 For a number of CEST profiles, including F88 and N102, we do see two dips/asymmetry
609 in the CEST traces (Extended Data Figs. 4d and 5d) and can, therefore, determine the chemical
610 shift of all three states. The CEST data for these residues could be fitted to the BAC-model, with
611 rate constants and populations very similar obtained for the “pure” two-state exchange models,
612 indicating that the observed profiles are caused by these two, independent, slow-exchange
613 processes. For others only one dip was visible, and there we determined the best initial value for
614 $\Delta\omega$ of the second minor state by starting from the two possible options (i.e., the chemical shift of
615 the other minor state is either close to the major state or to observable minor state) and comparing
616 the χ^2_{red} value.

617 Finally, a global fit and 400-500 Monte-Carlo runs were performed with every exchanging
618 residue and now allowing all parameters [$k_{ex,AB}/p_B$; $k_{ex,AC}/p_C$ (global) and $\Delta\omega_{AB}$, $\Delta\omega_{AC}$, R_1 , R_2 ,
619 ΔR_2 and I_0 (residue-specific)] to float. The results of this Monte-Carlo analysis are shown in
620 Extended Data Figs. 4e and 5e for k_{ex} /population and chemical shift differences are plotted on the
621 CypA structure (Extended Data Figs. 4f and 5f). Furthermore, assuming a three-state exchange
622 model, the χ^2_{red} and fitted R_2 values for exchanging residues went down to their expected values,
623 with the exception of the loop region undergoing exchange on the millisecond timescale that still
624 exhibits high R_2 values (Extended Data Figs. 4f and 5f).

625

626 **Data Availability.** Structure factors and refined model of CypA S99T/C115S/I97V has been
627 deposited in the PDB under accession code 5WC7. The NMR assignments of CypA S99T/C115S
628 and S99T/C115S/I97V have been deposited in the BMRB under accession codes 27217 and 27218,
629 respectively.

630

631 **Acknowledgements**

632 We thank N. Ollikainen, T. Kortemme and H. van den Bedem for discussions. We are grateful to
633 L. Kay, R. Muhandiram and G. Bouvignies for sharing their NMR pulse sequence codes and help
634 with the ChemEx software. F. Pontiggia is acknowledged for his help to implement the NMR data
635 fitting workflow on the Brandeis HPC cluster. We thank G. Coaker for AvrRpt2 constructs. This
636 work was supported by the Howard Hughes Medical Institute, the Office of Basic Energy Sciences,
637 Catalysis Science Program, U.S. Dept. of Energy, award DE-FG02-05ER15699 and NIH
638 (GM100966) to D.K., and a Searle Scholar Award from the Kinship Foundation, a Pew Scholar
639 Award from the Pew Charitable Trusts, a Packard Fellowship from the David and Lucile Packard
640 Foundation, NIH (GM110580), and NSF (STC-1231306) to J.S.F. R.O. was supported as an
641 HHMI Fellow of the Damon Runyon Cancer Research Foundation (DRG-2114-12). Data
642 collection at BL831 at the Advanced Light Sources is supported by the Director, Office of Science,
643 Office of Basic Energy Sciences, of the U.S. Department of Energy under Contract No. DE-AC02-
644 05CH11231, UC Office of the President, Multicampus Research Programs and Initiatives grant
645 MR-15-32859, and the Program Breakthrough Biomedical Research, which is partially funded by
646 the Sandler Foundation.

647

648 **Author Contributions**

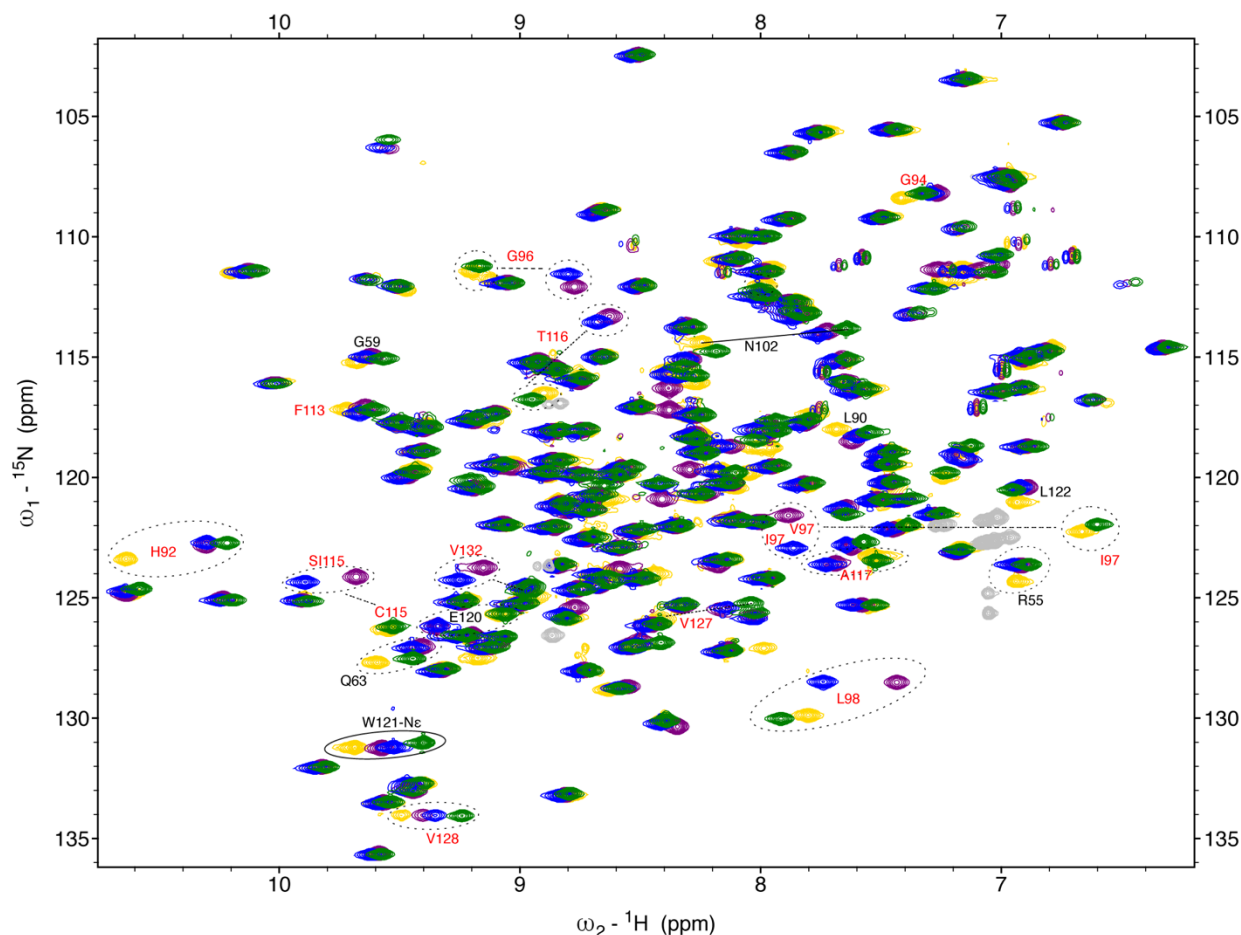
649 R.O., L.L., D.K. and J.S.F. designed experiments. L.L. and D.M. performed the library screen and
650 developed the assay for screening activity in cell lysate with supervision of D.S.T. and J.S.F.
651 L.L. performed the activity assay and R.O. analysed the data. L.L., L.R.K. and J.S.F. performed
652 the X-ray experiments; R.O. and M.W.C. performed the NMR experiments and R.O. analysed the
653 data. R.O., J.S.F. and D.K. wrote the paper. All authors contributed to data interpretation and
654 commented on the manuscript. Correspondence and requests for materials should be addressed to
655 J.S.F. (jfraser@fraserlab.com) or D.K. (dkern@brandeis.edu).

656

657

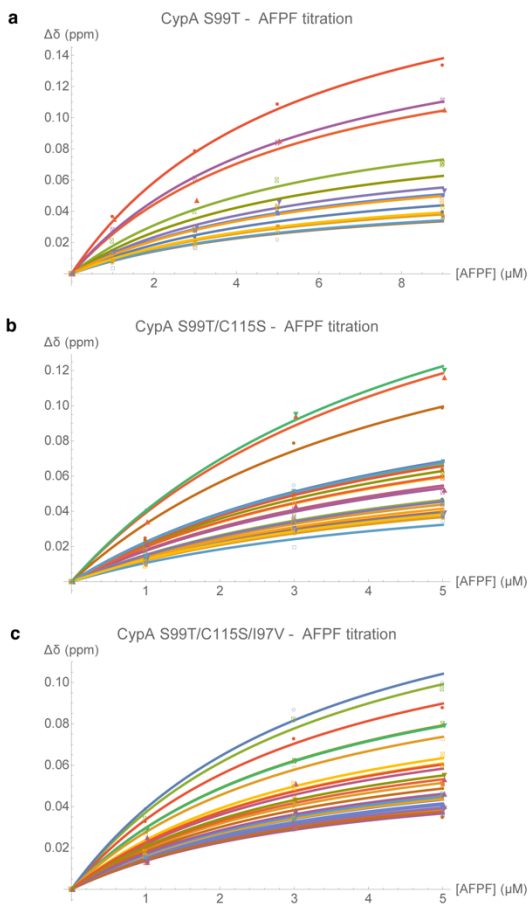
658 **Extended Data Figure 1 | Overlay of ^{15}N -[TROSY]-HSQC spectra for wild-type CypA**
659 **(yellow), S99T (green) and rescue mutants (S99T/C115S, blue; S99T/C115S/I97V, purple).**

660 All spectra were recorded on ~1 mM protein samples using a 600 MHz spectrometer at 10 °C.
661 Sequence-specific assignments given in red indicate residues that have moved significantly due to
662 proximity, in sequence and/or space, to the mutation site (<5 Å). Cross peaks connected with a
663 solid line or in a solid circle show the population inversion upon the Ser99 mutation and the partial
664 shift towards wild-type for the rescue mutants. Aliased Arg-N ϵ side chain signals are shown in
665 grey for all spectra.



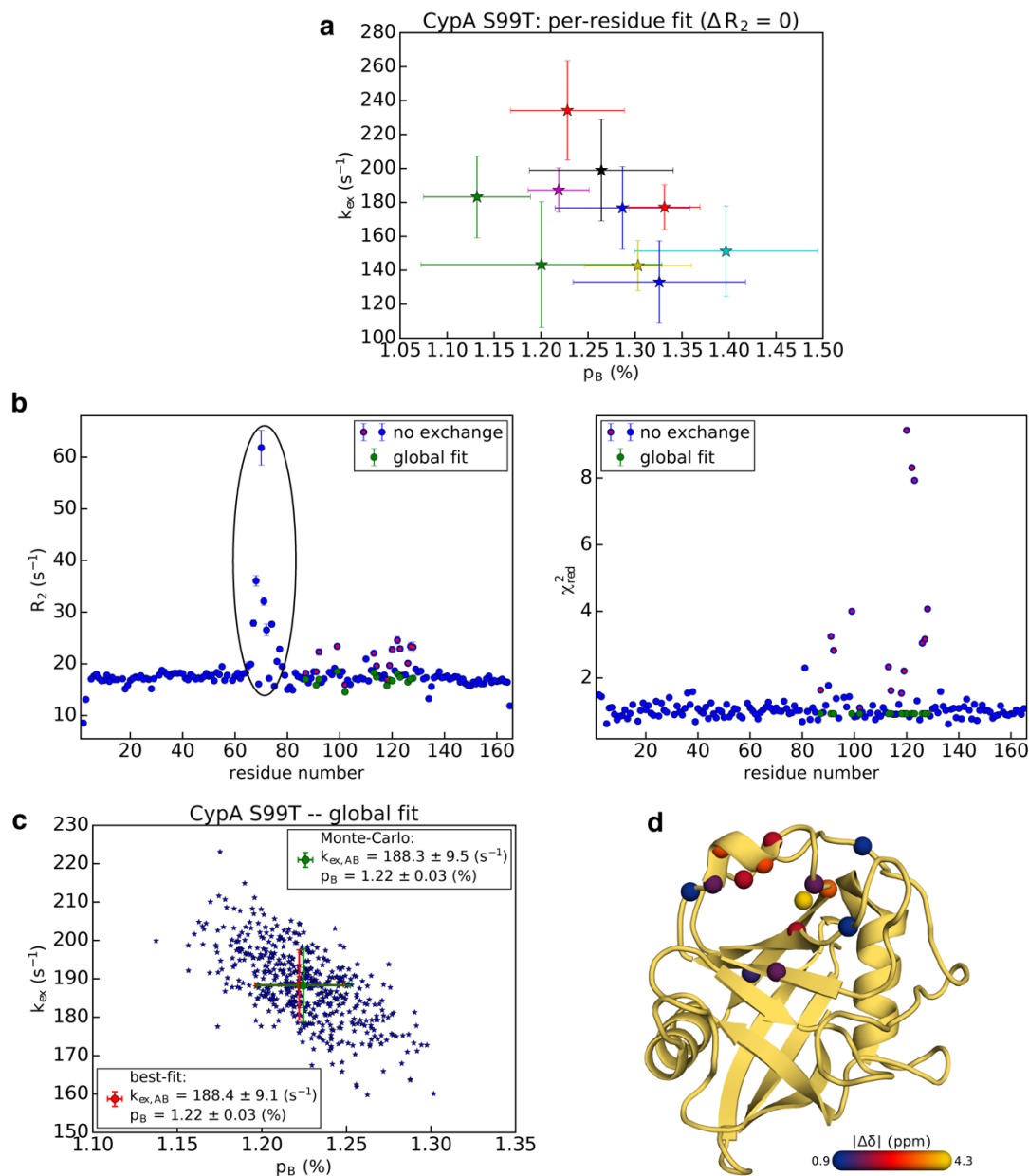
666

667 **Extended Data Figure 2 | K_D determination for the three mutant forms of CypA for Suc-**
 668 **AFPF-pNA measured by NMR chemical shift analysis from peptide titrations.** Resonances
 669 for which $\Delta\delta \geq 0.035$ ppm (thirteen for CypA S99T (a), twenty-three for S99T/C115S (b) and
 670 twenty-six for S99T/C115S/I97V (c), respectively) were fit simultaneously in Mathematica 11⁵⁰
 671 and standard errors are obtained from the global fit.

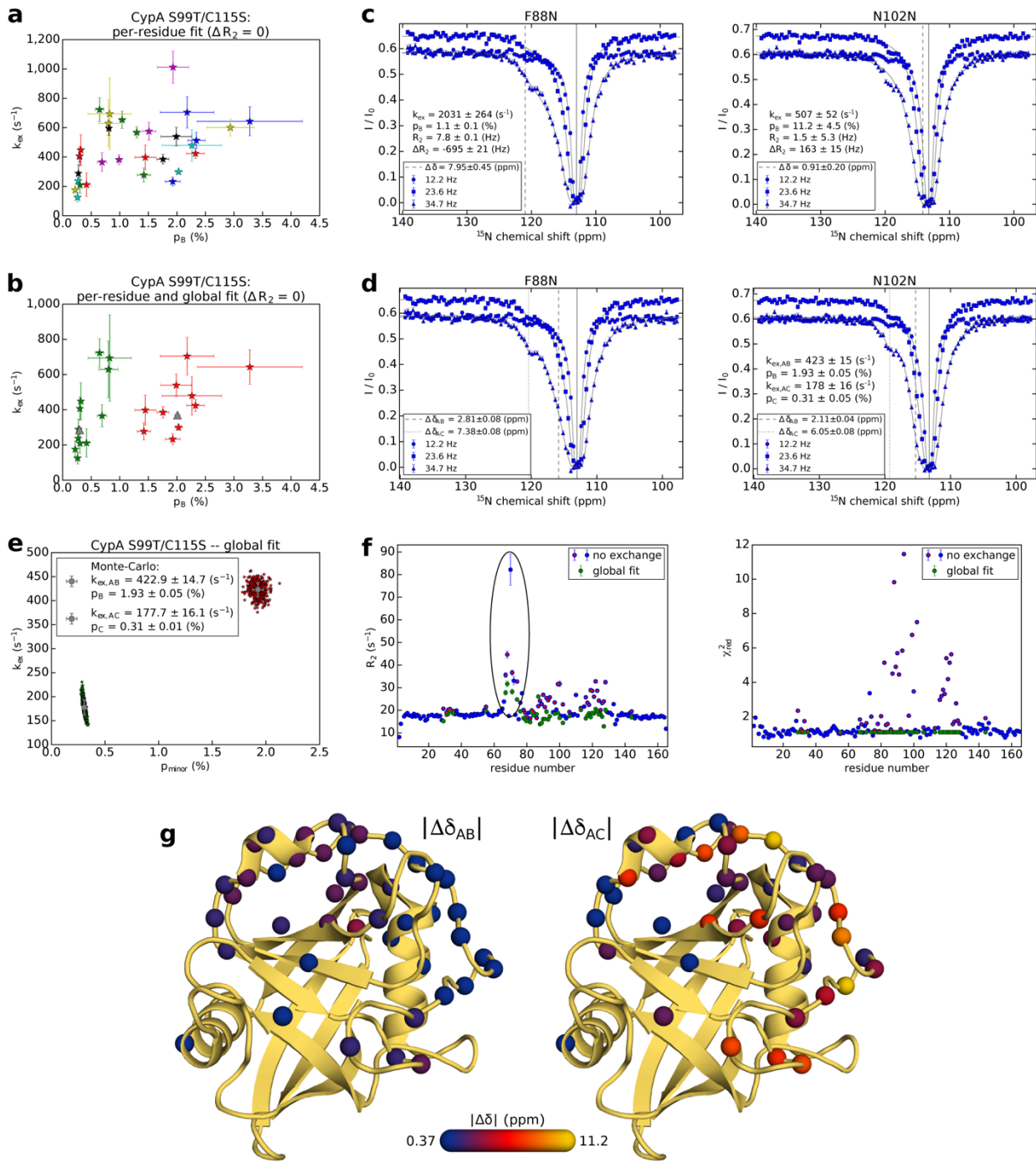


672
 673 **Extended Data Figure 3 | Analysis of the ^{15}N -CEST data for CypA S99T.** (a) Per-residue fit of
 674 the CEST profiles for the initial 10 residues that clearly show slow exchange by visual inspection.
 675 Clustering of the k_{ex}/p_B values indicate the presence of one global exchange process. (b)
 676 Comparison of R_2 and χ^2_{red} values for no-exchange model (blue) and one global, slow-exchange

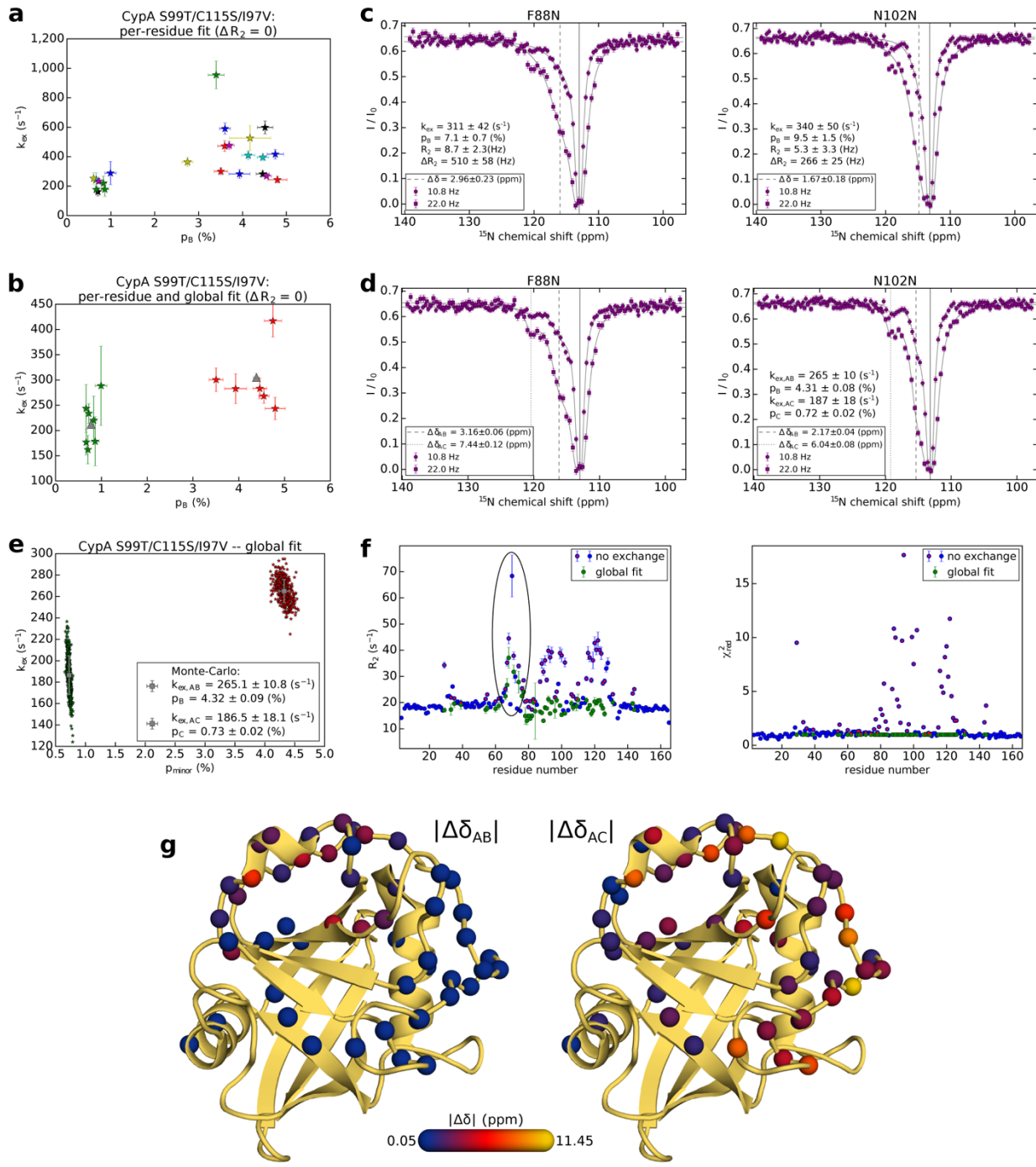
677 process (green). For ease of comparison residues that are included in the global fit are also shown
678 with a red marker for the no-exchange model. Fitting the data assuming no exchange results in
679 elevated R_2 values (left) for the loop region (residues 65-80), whereas χ^2_{red} values (right) are close
680 to one. This observation is consistent with line broadening of the ground-state signal due to
681 dynamics on the millisecond timescale and the absence of a second dip or asymmetry that would
682 indicate a slow-exchange process. In contrast, assuming a no-exchange model for residues that, in
683 fact, do experience a slow-exchange process, results in large χ^2_{red} values in addition to a higher R_2
684 in an attempt to –unsuccessfully– explain the asymmetry in the CEST profiles. The data show that
685 the data can be explained satisfactorily by one, global exchange process as judged from the R_2 and
686 χ^2_{red} values. **(c)** Uncertainties in the fitting parameters for the global fit were determined from 500
687 Monte-Carlo simulations and the resulting scatter plot for k_{ex} vs. p_B is shown. The values and their
688 uncertainties obtained using this method and estimated from the covariance matrix are nearly
689 identical. **(d)** The chemical shift difference between the states, $|\Delta\delta|$, for the 15 residues is plotted
690 on the structure of CypA.



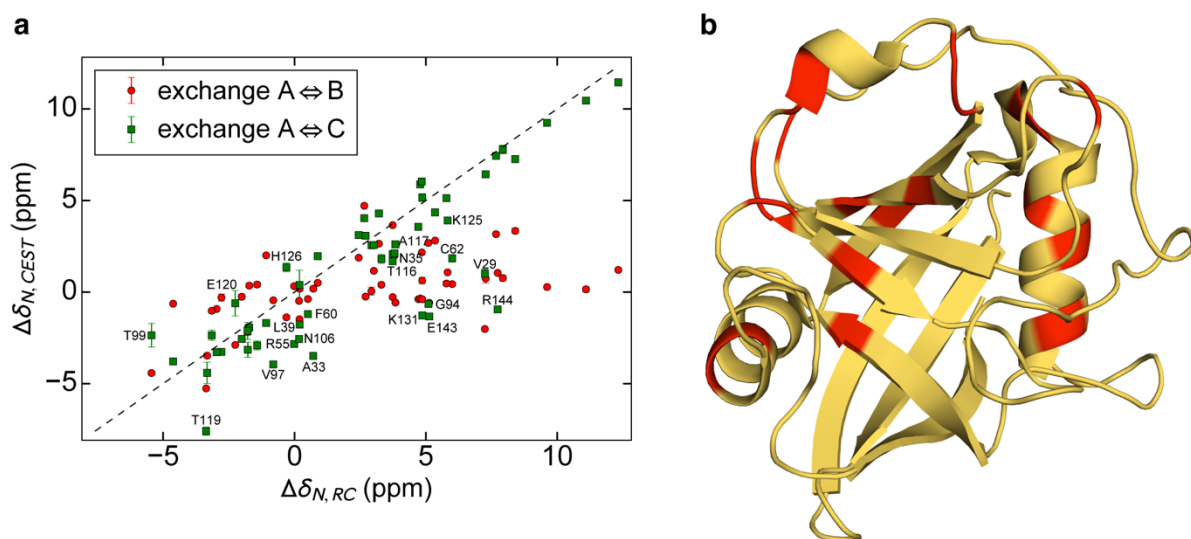
692 **Extended Data Figure 4 | Analysis of the ^{15}N -CEST data for CypA S99T/S115S indicates the**
693 **presence of more than one exchange process.** (a) Per-residue fit of the CEST profiles for the
694 initial 30 residues that clearly show slow exchange by visual inspection. Clustering of the k_{ex}/p_B
695 values suggests the presence of two distinct exchange processes. (b) Residues that are well-
696 described by a two-state exchange model were split into two clusters (*c.f.*, red (11 residues) and
697 green (22 residues) spheres in Fig. 2e). Here, only the residues that are present in panel a and are
698 used in the two-state global fit are shown together with their respective global k_{ex}/p_B values (grey
699 triangles). (c-d) Several residues, including F88 and N102, do not fit to a two-site exchange process
700 even if all fitting parameters are allowed to float (c). However, a three-site exchange model can
701 explain the experimental data (d) and the vales of $k_{\text{ex}}/p_{\text{minor}}$ correspond well to the two observed
702 clusters assuming a single two-site exchange model (panel b). (e) Uncertainties in the fitting
703 parameters for the three-state global fit that include all 46 residues were determined from 400
704 Monte-Carlo simulations and the resulting scatter plot for k_{ex} vs. p_{minor} is shown. The values and
705 their uncertainties obtained using this method and from the covariance matrix are nearly identical.
706 (f) Residue-specific values of R_2 and χ^2_{red} assuming there is no exchange (blue) or a global, three-
707 site process (green). For ease of comparison, the 46 residues that experience exchange and are
708 included in the global fit are also shown with a red marker for the no-exchange model. Fitting a
709 no-exchange model shows significantly elevated R_2 and χ^2_{red} values for a large number of residues.
710 After fitting an appropriate exchange model R_2 and χ^2_{red} drop to expected values, with the
711 exception of the loop region (residues 65-80), where elevated R_2 values are still observed,
712 consistent with line broadening of the ground-state signal due to dynamics on the millisecond
713 timescale. (g) The chemical shift differences between the states, $|\Delta\delta_{AB}|$ (left panel) and $|\Delta\delta_{AC}|$ (right
714 panel), for the 46 residues are plotted on the structure of CypA.



716 **Extended Data Figure 5 | Analysis of the ^{15}N -CEST data for CypA S99T/S115S/I97V**
717 **indicates the presence of more than one exchange process.** (a) Per-residue fit of the CEST
718 profiles for the initial 23 residues that clearly show slow exchange by visual inspection. Clustering
719 of the k_{ex}/p_B values suggest the presence of two distinct exchange processes. (b) Residues that are
720 well-described by a two-state exchange model were split into two clusters (*c.f.*, red (12 residues)
721 and green (25 residues) spheres in Fig. 2g). Here, only the residues that are in panel a and are used
722 in the two-state global fit are shown together with their respective global k_{ex}/p_B values (grey
723 triangles). (c-d) Several residues, including F88 and N102, do not fit to a two-site exchange process
724 even if all fitting parameters are allowed to float (c). However, a three-site exchange model can
725 explain the experimental data (d) and the vales of $k_{\text{ex}}/p_{\text{minor}}$ correspond well to the two observed
726 clusters assuming a single two-site exchange model (panel b). (e) Uncertainties in the fitting
727 parameters for the three-state global fit that include all 55 residues were determined from 425
728 Monte-Carlo simulations and the resulting scatter plot for k_{ex} vs. p_{minor} is shown. The values and
729 their uncertainties obtained using this method and from the covariance matrix are nearly identical.
730 (f) Residue-specific values of R_2 and χ^2_{red} assuming there is no exchange (blue) or a global, three-
731 site process (green). For ease of comparison, the 55 residues that experience exchange and are
732 included in the global fit are also shown with a red marker for the no-exchange model. Fitting a
733 no-exchange model shows significantly elevated R_2 and χ^2_{red} values for a large number of residues.
734 After fitting an appropriate exchange model R_2 and χ^2_{red} drop to expected values, with the
735 exception of the loop region (residues 65-80), where elevated R_2 values are still observed,
736 consistent with line broadening of the ground-state signal due to dynamics on the millisecond
737 timescale. (g) The chemical shift differences between the states, $|\Delta\delta_{AB}|$ (left panel) and $|\Delta\delta_{AC}|$ (right
738 panel), for the 55 residues are plotted on the structure of CypA.

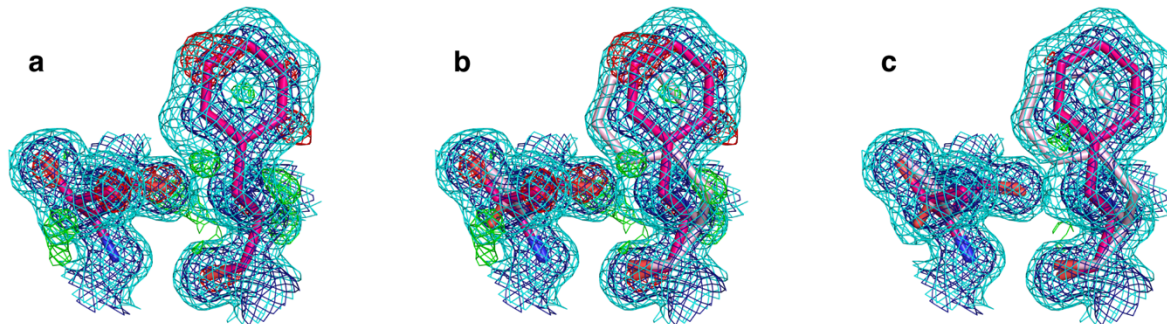


740 **Extended Data Figure 6 | Correlation between ^{15}N $\Delta\delta$ values obtained from CEST and those**
 741 **between the major state and predicted random coil chemical shifts of CypA**
 742 **S99T/C115S/I97V.** (a) ^{15}N chemical shift differences between state A \leftrightarrow B (red circles) and A \leftrightarrow C
 743 (green squares) were extracted from the 3-state global fit of the CEST profiles, and the random
 744 coil chemical shifts were predicted using the method of Tamiola *et al.*⁵⁸. There is no clear
 745 correlation between $\Delta\delta_{\text{N},\text{AB}}$ and $\Delta\delta_{\text{N},\text{RC}}$ (pairwise rmsd = 4.2 ppm). On the contrary, the correlation
 746 between $\Delta\delta_{\text{AC}}$ and $\Delta\delta_{\text{RC}}$ suggests that minor state C corresponds to a more extended/unfolded
 747 conformation. Residues that are labeled with their assignment are not correlated ($|\Delta\delta_{\text{N},\text{AC}}-\Delta\delta_{\text{N},\text{RC}}|$
 748 ≥ 1.5 ppm), indicating that these do not sample an extended conformation, and are color in red on
 749 the structure (b). The majority of these residues belong to group-I or are part of the dynamic
 750 network that is involved in the catalysis. The pairwise rmsd for $\Delta\delta_{\text{N},\text{AC}}$ and $\Delta\delta_{\text{N},\text{RC}}$ is 2.6 ppm when
 751 considering all residues and 0.9 ppm excluding the labeled ones that are part of the dynamic
 752 network.



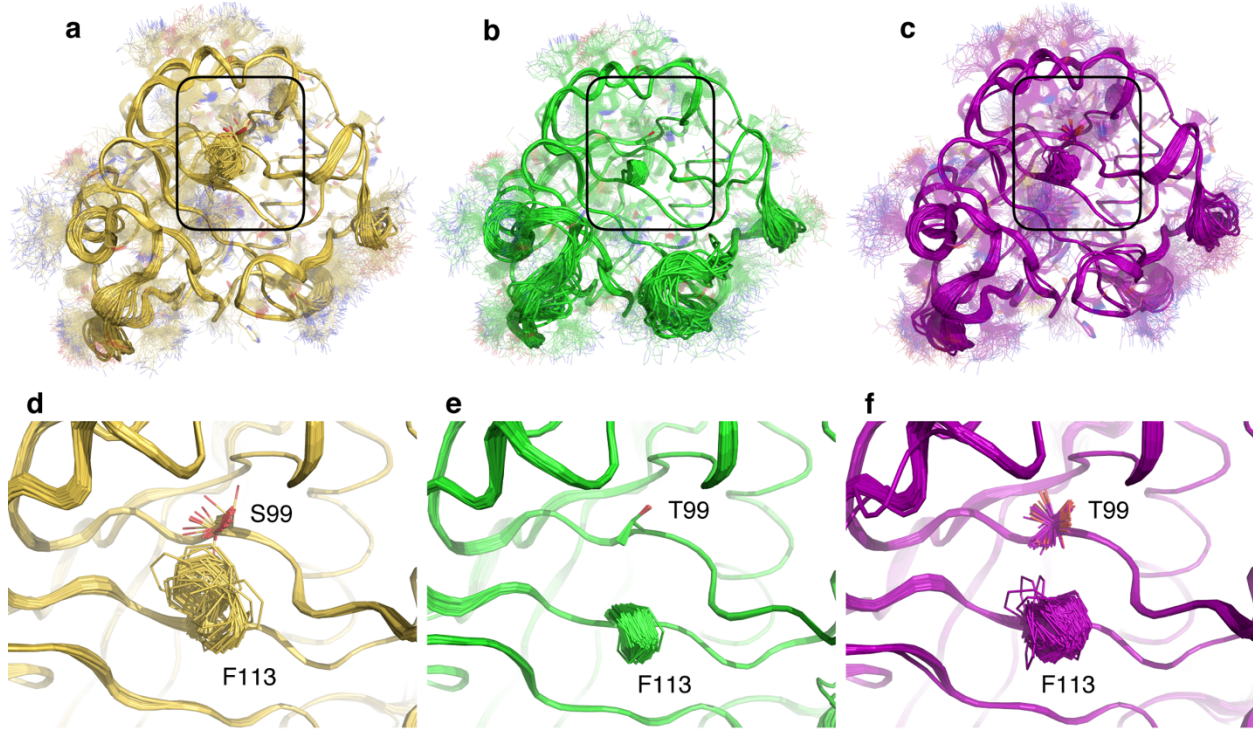
753

754 **Extended Data Figure 7 | Difference electron density for alternative conformations of Thr99**
755 **and Phe113 in CypA S99T/C115S/I97V.** (a) Negative and positive difference peaks in mFo-DFc
756 electron density ($\pm 3.0\sigma$ in green and red) are contained within expanded 2mFo-DFc electron
757 density (2.0 σ in dark blue and 0.3 σ in cyan), and not accounted for by a single conformer model
758 (magenta) of CypA S99T/C115S/I97V. (b) The electron density maps as shown in (a) with the
759 refined qFit multiconformer model (alternative conformations in magenta, ~0.8 occupancy, and
760 light pink, ~0.2 occupancy) that explains the difference features. (c) The refined qFit models
761 shown in (b) with the final 2mFo-DFc (2.0 σ in dark blue and 0.3 σ in cyan) and mFo-DFc maps
762 ($\pm 3.0\sigma$ in green and red).



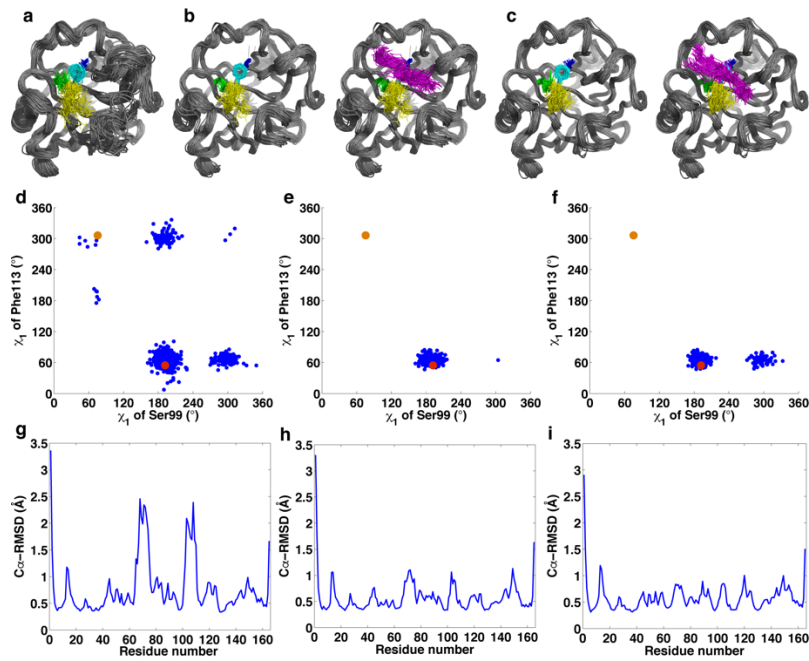
763
764 **Extended Data Figure 8 | Time-averaged ensemble refinement for wild-type CypA (yellow),**
765 **S99T (green), and S99T/C115S/I97V (purple).** All refinements were performed using
766 phenix.ensemble refinement³⁸ with parameters (pTLS, wxray, tx) selected based on lowest R_{free}.
767 Overall view (a-c) and corresponding zoom-in (d-f) for wild-type CypA (a,d) (refined with pTLS
768 0.775, wxray 8.125, and tx 2.0) shows extensive side chain heterogeneity in the active site
769 extending to the core through residues Phe113 and Ser99 (shown in sticks); S99T (b,e) (refined
770 with pTLS 0.775, wxray 8.125, and tx 2.0) shows no heterogeneity in Phe113 and Thr99; and

771 S99T/C115S/I97V (**c,f**) (refined with pTLS 0.55, wxray 8.125, and tx 2.0) shows increased
772 heterogeneity in Phe113 and multiple conformations of Thr99 relative to the S99T.



774 **Extended Data Figure 9 | Analysis of conformational ensembles calculated by Camilloni et**
775 **al. using DFT calculations to propose a catalytic mechanism²⁶.** Conformational heterogeneity
776 is suppressed in the catalytic complexes, and alternate conformations seen in the X-ray structures¹¹
777 are not sampled in the simulation with the substrates bound. **(a-c)** A subset of 68 randomly selected
778 ensemble members is shown in cartoon with residues Ser99 (blue), Phe113 (cyan), Met61 (green),
779 and Arg55 (yellow) shown in sticks. The apo protein ensemble **(a)** shows more conformational
780 heterogeneity than the peptide (GSFGPDLRAGD) substrate-bound forms with a Gly-Pro in cis-
781 (**b**) and trans- (**c**) conformations, shown without (left) or with (right) the substrate backbone
782 (magenta). Curiously, their cis- and trans-peptide complexes show only minimal protein
783 conformational differences compared to the starting crystal structures, while the free CypA showed
784 multiple substates in their simulations. This is reflected in the dihedral angle distribution for Ser99

785 and Phe113 for apo wild-type CypA (**d**) versus the cis- (**e**) and trans- (**f**) substrate bound
 786 ensembles. The two alternative (major and minor) conformations seen in the room-temperature X-
 787 ray structure of wild-type CypA (PDB 3k0n) are shown in as red and orange dots for reference.
 788 Their result is in sharp contrast with our NMR dynamics for WT¹⁰ and S99T during catalysis
 789 measured here, which clearly shows that conformational substates interconvert across the core
 790 catalytic network and that this rate is correlated to catalysis. Although no significant change in
 791 loop dynamics is detected by NMR during catalysis, the MD simulations indicate larger deviations
 792 in the C^α RMSDs in the apo protein (**g**) is specifically decreased in the loops surrounding residues
 793 60-80 and 100-120 in the cis- (**h**) and trans- (**i**) substrate bound ensembles. New simulations that
 794 incorporate the side-chain dynamics characterized here may help bridging their DFT
 795 computational approach which emphasize a key role for electrostatics, with our experimental
 796 results that deliver the protein conformational substates.



797

798

799 **Extended Data Table 1 | Data collection and refinement statistics.**

800 The number of crystals for each structure is 1.

801 * Values in parentheses are for highest-resolution shell.

CypA S99T/C115S/I97V (5WC7)	
Data collection	
Space group	P212121
Cell dimensions	
a, b, c (Å)	43.0, 52.4, 89.2
α, β, γ (°)	90, 90, 90
Resolution (Å)	33.97 – 1.43 (1.48 – 1.43)*
R_{merge}	0.031 (0.482)
$I/\sigma(I)$	18.7 (1.1)
$CC_{1/2}$	1 (0.829)
Completeness (%)	0.99 (0.96)
Redundancy	3.81 (2.37)
Refinement	
Resolution (Å)	33.21 – 1.43
No. reflections	37777 (3735)
$R_{\text{work}} / R_{\text{free}}$	0.1031/0.1285
No. atoms	
Protein	2023
Water	229
B factors	
Protein	19.88
Water	43.71
R.m.s. deviations	
Bond lengths (Å)	0.010
Bond angles (°)	1.26

802

803

804 **References:**

805

- 806 31 Rockah-Shmuel, L., Toth-Petroczy, A. & Tawfik, D. S. Systematic Mapping of Protein
807 Mutational Space by Prolonged Drift Reveals the deleterious Effects of Seemingly
808 Neutral Mutations. *PLoS Comput Biol* **11**, e1004421, doi:10.1371/journal.pcbi.1004421
809 (2015).
- 810 32 Kabsch, W. Xds. *Acta Crystallogr D Biol Crystallogr* **66**, 125-132,
811 doi:10.1107/S0907444909047337 (2010).

- 812 33 Keedy, D. A. *et al.* Mapping the conformational landscape of a dynamic enzyme by
813 multitemperature and XFEL crystallography. *eLife* **4**, doi:10.7554/eLife.07574 (2015).
- 814 34 Karplus, P. A. & Diederichs, K. Linking crystallographic model and data quality. *Science*
815 **336**, 1030-1033, doi:10.1126/science.1218231 (2012).
- 816 35 McCoy, A. J. *et al.* Phaser crystallographic software. *J Appl Crystallogr* **40**, 658-674,
817 doi:10.1107/S0021889807021206 (2007).
- 818 36 Emsley, P., Lohkamp, B., Scott, W. G. & Cowtan, K. Features and development of Coot.
819 *Acta Crystallogr D Biol Crystallogr* **66**, 486-501, doi:10.1107/S0907444910007493
820 (2010).
- 821 37 Afonine, P. V. *et al.* Towards automated crystallographic structure refinement with
822 phenix.refine. *Acta Crystallogr D Biol Crystallogr* **68**, 352-367,
823 doi:10.1107/S0907444912001308 (2012).
- 824 38 Burnley, B. T., Afonine, P. V., Adams, P. D. & Gros, P. Modelling dynamics in protein
825 crystal structures by ensemble refinement. *eLife* **1**, e00311, doi:10.7554/eLife.00311
826 (2012).
- 827 39 The PyMOL Molecular Graphics System v. 1.8.6 (2017).
- 828 40 Delaglio, F. *et al.* NMRPipe: a multidimensional spectral processing system based on
829 UNIX pipes. *J Biomol Nmr* **6**, 277-293, doi:Doi 10.1007/Bf00197809 (1995).
- 830 41 Lee, W., Tonelli, M. & Markley, J. L. NMRFAM-SPARKY: enhanced software for
831 biomolecular NMR spectroscopy. *Bioinformatics* **31**, 1325-1327,
832 doi:10.1093/bioinformatics/btu830 (2015).
- 833 42 Muhandiram, D. R. & Kay, L. E. Gradient-Enhanced Triple-Resonance Three-
834 Dimensional NMR Experiments with Improved Sensitivity. *Journal of Magnetic
835 Resonance, Series B* **103**, 203-216, doi:10.1006/jmrb.1994.1032 (1994).

- 836 43 Grzesiek, S. & Bax, A. Correlating backbone amide and side chain resonances in larger
837 proteins by multiple relayed triple resonance NMR. *Journal of the American Chemical
838 Society* **114**, 6291-6293, doi:10.1021/ja00042a003 (1992).
- 839 44 Kay, L., Keifer, P. & Saarinen, T. Pure absorption gradient enhanced heteronuclear
840 single quantum correlation spectroscopy with improved sensitivity. *Journal of the
841 American Chemical Society* **114**, 10663-10665, doi:10.1021/ja00052a088 (1992).
- 842 45 Weigelt, J. Single Scan, Sensitivity- and Gradient-Enhanced TROSY for
843 Multidimensional NMR Experiments. *Journal of the American Chemical Society* **120**,
844 10778-10779, doi:10.1021/ja982649y (1998).
- 845 46 Zhang, O., Kay, L. E., Olivier, J. P. & Forman-Kay, J. D. Backbone 1H and 15N
846 resonance assignments of the N-terminal SH3 domain of drk in folded and unfolded
847 states using enhanced-sensitivity pulsed field gradient NMR techniques. *J Biomol Nmr* **4**,
848 845-858 (1994).
- 849 47 Ulrich, E. L. et al. BioMagResBank. *Nucleic Acids Res* **36**, D402-408,
850 doi:10.1093/nar/gkm957 (2008).
- 851 48 Ahlner, A., Carlsson, M., Jonsson, B. H. & Lundstrom, P. PINT: a software for integration
852 of peak volumes and extraction of relaxation rates. *J Biomol Nmr* **56**, 191-202,
853 doi:10.1007/s10858-013-9737-7 (2013).
- 854 49 Mulder, F. A., Schipper, D., Bott, R. & Boelens, R. Altered flexibility in the substrate-
855 binding site of related native and engineered high-alkaline *Bacillus subtilisins*. *J Mol Biol*
856 **292**, 111-123, doi:10.1006/jmbi.1999.3034 (1999).
- 857 50 Mathematica (Wolfram Research, Inc., Champaign, Illinois, 2017).
- 858 51 Loria, J. P., Rance, M. & Palmer, A. G. A Relaxation-Compensated
859 Carr-Purcell-Meiboom-Gill Sequence for Characterizing Chemical Exchange by NMR
860 Spectroscopy. *Journal of the American Chemical Society* **121**, 2331-2332,
861 doi:10.1021/ja983961a (1999).

- 862 52 Tollinger, M., Skrynnikov, N. R., Mulder, F. A., Forman-Kay, J. D. & Kay, L. E. Slow
863 dynamics in folded and unfolded states of an SH3 domain. *J Am Chem Soc* **123**, 11341-
864 11352, doi:10.1021/ja011300z (2001).
- 865 53 Mulder, F. A. A., Skrynnikov, N. R., Hon, B., Dahlquist, F. W. & Kay, L. E. Measurement
866 of Slow (μ s-ms) Time Scale Dynamics in Protein Side Chains by ^{15}N Relaxation
867 Dispersion NMR Spectroscopy: Application to Asn and Gln Residues in a Cavity Mutant
868 of T4 Lysozyme. *Journal of the American Chemical Society* **123**, 967-975,
869 doi:10.1021/ja003447g (2001).
- 870 54 Mulder, F. A., Hon, B., Mittermaier, A., Dahlquist, F. W. & Kay, L. E. Slow internal
871 dynamics in proteins: application of NMR relaxation dispersion spectroscopy to methyl
872 groups in a cavity mutant of T4 lysozyme. *J Am Chem Soc* **124**, 1443-1451,
873 doi:10.1021/jp0119806 (2002).
- 874 55 Guenneugues, M., Berthault, P. & Desvaux, H. A method for determining B1 field
875 inhomogeneity. Are the biases assumed in heteronuclear relaxation experiments usually
876 underestimated? *J Magn Reson* **136**, 118-126, doi:10.1006/jmre.1998.1590 (1999).
- 877 56 McConnell, H. M. Reaction Rates by Nuclear Magnetic Resonance. *J Chem Phys* **28**,
878 430-431, doi:Doi 10.1063/1.1744152 (1958).
- 879 57 Sekhar, A. et al. Thermal fluctuations of immature SOD1 lead to separate folding and
880 misfolding pathways. *eLife* **4**, e07296, doi:10.7554/eLife.07296 (2015).
- 881 58 Tamiola, K., Acar, B. & Mulder, F. A. Sequence-specific random coil chemical shifts of
882 intrinsically disordered proteins. *J Am Chem Soc* **132**, 18000-18003,
883 doi:10.1021/ja105656t (2010).